Pacific Northwest
NATIONAL LABORATORY

PNNL-32400

Prediction of Aluminum to Steel RSW Joint Failure (CRADA 405)

A Finite Element Modeling Approach

December 2021

Kyoo Sil Choi
Christopher B Smith
Wenbin Kuang
Nicole R Overman
Xiaolong Ma
Wayne Cai (General Motors)
Blair E Carlson (General Motors)

U.S. DEPARTMENT OF ENERGY

Prepared for the U.S. Department of Energy
under Contract DE-AC05-76RL01830

PACIFIC NORTHWEST NATIONAL LABORATORY
operated by
BATTELLE
for the
UNITED STATES DEPARTMENT OF ENERGY
under Contract DE-AC05-76RL01830

Printed in the United States of America

Available to DOE and DOE contractors from the
Office of Scientific and Technical Information,
P.O. Box 62, Oak Ridge, TN 37831-0062;
ph: (865) 576-8401
fax: (865) 576-5728
email: reports@adonis.osti.gov

Available to the public from the National Technical Information Service
5301 Shawnee Rd., Alexandria, VA 22312
ph: (800) 553-NTIS (6847)
email: orders@ntis.gov <https://www.ntis.gov/about>
Online ordering: http://www.ntis.gov

PNNL-32400

Prediction of Aluminum to Steel RSW Joint Failure

A Finite Element Modeling Approach

December 2021

Kyoo Sil Choi
Christopher B Smith
Wenbin Kuang
Nicole R Overman
Xiaolong Ma
Wayne Cai (General Motors)
Blair E Carlson (General Motors)

Prepared for
the U.S. Department of Energy
under Contract DE-AC05-76RL01830

Pacific Northwest National Laboratory
Richland, Washington 99354

Summary

Resistance spot welding (RSW) is commonly used as a joining process at automotive original equipment manufacturers (OEMs) for body-in-white manufacturing where material thicknesses are typically 0.5 to 3.0 mm. Historically, RSW has been used to similar metal combinations (e.g., steel to steel). Given the widespread use of RSW, there is desire to use the process for dissimilar material combinations (e.g., aluminum to steel) to enable weight reductions. General Motors has performed considerable work to overcome various metallurgical challenges associated with dissimilar material joining. GM has demonstrated that RSW can effectively create joints of sufficient strength between aluminum and steel. Two different weld failure modes (i.e., button pull-out and interface failure) in RSW are primarily observed. Currently, these failure modes can only be determined via costly destructive tensile tests. There is no means for predicting these failure modes. Further, it is unknown which materials, stack-up, or welding conditions are most contributive to the failure mode of the aluminum to steel joints.

In this study, it was envisioned that finite element (FE) methods could be used to predict the failure modes of aluminum to steel RSWs subjected to various tensile test methods. For this purpose, the weld coupons were first made with various material combinations. The coupons were then tested under different destructive testing configurations. Microstructural characterization and micro/nano indentation tests were also performed to evaluate the local material properties within the weld nugget region. Resistance spot weld simulation FE models were generated/simulated for a selected material combination based on the estimated local material property data sets in order to examine the influence of various aspects on the failure modes and load-extension curves. The model validation efforts have also been performed after fine-tuning the material parameters.

The results from the tensile destructive tests show that the failure modes can be different for different material combinations, and also be often changed with application of baking process. The results of the simulation tasks for failure mode prediction show that the IMC fracture strength may be decreased with baking process, indicating that the bonding strength of IMC layer may be weakened possibly due to some local cacking along the interface during baking process. Aluminum fracture strain curves, estimated based on tensile test and limiting dome height test, were then used and fine-tuned in order to capture the load-extension curves and failure modes of the samples for different test configurations and baking conditions. The results of the model validation efforts show that the fine-tuned fracture strain curves for aluminum can adequately predict the load-extension curves and failure mode for lap shear (LS) tensile testing. However, there is some noticeable discrepancy for coach peel (CP) tensile testing as compared to experiments. Further fine-tuning efforts need to be done to validate the current modeling method.

Acknowledgments

This work was conducted under a Cooperative Research and Development Agreement, CRADA #PNNL-405 between General Motors and the Pacific Northwest National Laboratory. The authors would like to acknowledge sponsorship by the Department of Energy, Vehicle Technologies Office under the LightMAT Consortium. Special thanks to Ms. Sarah Kleinbaum for supporting this research work. The authors would like to thank and recognize Dr. Shawn Riechers, a PNNL staff member, for atomic force microscopy testing and input, and Dr. Amberlee Haselhuhn, a former General Motors staff member, for providing her insight and various coupon test data. All the experimental works and material provisions from General Motors for this project are also appreciated here.

Acronyms and Abbreviations

0BK	unbaked coupons
1BK	single baked processed
2BK	twice baked processed
BIW	body-in-white
BK	baking
BP	button pull-out failure
CP	coach peel
CR	cold-rolled steel
CT	cross tension
CTE	coefficient of thermal expansion
EBSD	electron backscatter diffraction
EDS	energy dispersive spectroscopy
FE	finite element
FT	face tear failure
HAZ	heat affected zone
HB	half button failure
HSLA	high strength low alloy steel
IF	interface failure
IMC	intermetallic compound
LCS	low carbon steel
LDH	limiting dome height test
LS	lap shear
MFDC	medium frequency direct current
MRD	multi-ring domed
OEM	original equipment manufacturer
PB	partial button failure
PHS	press hardened steel
RSW	resistance spot welding
SEM	scanning electron microscopy
SPR	self-piercing rivets
UTS	ultimate tensile strength

Contents

Figures

Tables

1.0 Introduction

In an effort to reduce vehicle mass, automakers are incorporating lightweight materials within vehicle bodies at an ever-increasing rate. The primary focus has been on incorporating ultra-high strength steels such as press hardened steels (PHS), complex phase steels, and others. Even further mass reductions can be achieved by incorporating aluminum or magnesium alloy materials such as sheet, extrusions, and castings into a multi-material body. However, structural joints comprised of dissimilar metals are generally difficult.

One solution to the challenge of joining non-ferrous alloys to steels is self-piercing rivets (SPR). Compared to traditional automotive style resistance spot welding, the use of SPRs can result in added vehicle mass, increased cost per joint (consumable cost/rivet), and increased equipment expenditures. Since SPRs will most likely be co-located with pre-existing resistance welding equipment in the body shop, their use will require additional floor space. However, joining of dissimilar materials with a single, common process can reduce equipment costs and floor space, but it also increases technical complexity.

Welding dissimilar metals adds to technical complexity for several reasons. For example, aluminum and steel exhibit vastly different melting temperatures: ~600°C versus ~1500°C, respectively. When resistance spot welding steel to aluminum, the steel at the joint interface does not melt, leading to lack of mixing between molten aluminum and steel. Aluminum and steel also possess different electrical and thermal conductivities and thermal expansion coefficients. The different electrical conductivities result in most of the heat generation occurring within the steel substrate during resistive heating. The different thermal properties affect their melting and solidification behavior, particularly the distribution of porosity during solidification. Ultimately, a weld is made with a thin layer of brittle aluminum-iron intermetallic that limits strength and ductility at the Al-Steel interface.

Considerable work has been performed by General Motors (GM) to overcome these metallurgical challenges [1]. Using a specially designed welding electrode and novel multi-stage welding schedules, it is possible to eliminate oxide films, consolidate porosity, and control intermetallic layer growth, effectively making a strong joint between aluminum and steel. Unlike traditional resistance spot welds comprised of the same material, dissimilar Al-Steel joints form a weld nugget only in the aluminum sheet while the steel sheet forms a heat affected zone but does not melt. Differences in heat input, joint geometry, sheet thickness, sheet deformation, and microstructural features have all been observed to impact mechanical properties. Furthermore, there are significant differences in the intermetallic compound (IMC) development between joints containing AA6XXX vs AA5XXX and, in general, peak fracture loads can vary by an order of magnitude for a given material combination depending upon whether the joint fractures at the interface or via button pullout. Traditionally, button pull-out (BP) failure mode, where the weld nugget remains on the lower sheet upon completion of a destructive test, is deemed to be a failure mode that is indicative of a quality joint as this mode has been demonstrated to absorb significant fracture energy. To the contrary, interface failure (IF) is considered an unacceptable mode as the joint typically fails early and rapidly at the interface resulting in much less energy absorption.

However, it is currently unclear specifically which factors are most critical for predicting joint fracture modes in these unique joints comprised of dissimilar aluminum and steel metals. This uncertainty translates to significant development time required when expanding this technology to additional combinations of alloys and sheet thicknesses. This project was proposed and initiated with the objective to develop a modeling method that could predict failure mode of the weld coupons of different material combinations under various destructive test configurations (i.e., coach peel, cross tension and lap shear). Additionally, automotive resistance spot welded components are often processed through paint-baking steps. This exposes the weld components to additional thermal history which has been demonstrated to have an effect on the joint failure mode of RSW joints of aluminum to steel. This thermal history effect is also an important factor that needs to be considered in the project.

While the overall objective of this project was to develop a validated finite element (FE) modeling method that can predict the failure mode of aluminum to steel resistance spot weld, four detailed tasks were set up to support this effort. They can be summarized as follows:

- Fabrication and Destructive Testing of Aluminum to Steel Spot Weld Coupons: This was a General Motors led effort that involved creating weld coupons in five different joint configurations. Post weld destructive testing included coach peel, cross tension and lap shear tests. In addition, micro hardness testing and metallography were included as part of this effort.

- Detailed Characterization of the Aluminum to Steel RSW Joints: This was a PNNL led effort focused on micro-structural characterization and local material property measurement. Outputs from effort would be inputs to the FE model.

- Weld Joint Simulation Finite Element Modeling: This was a PNNL led effort towards development of FE models to simulate the three destructive test configurations using material property data inputs.

- Validation: Validation efforts were performed to gauge the accuracy of the developed model. By comparing failure modes of the actual samples vs. the model prediction and analyzing discrepancies, additional model refinement activities were performed to improve the accuracy of the model.

In the project efforts, the weld simulation FE models in the 3rd task were generated and simulated to examine the influence of various aspects on the failure modes and load-extension curves. The model validation efforts in the 4th task have been performed with gradual refinement of material parameters. However, the model validation was not completed yet to the extent of satisfaction, and further work is expected to be done for its completeness. In this report, the key results and lessons learned so far from the project efforts are summarized in the sequence of tasks described above. Significant amount of experimental data as well as the technical challenges that the authors experienced in the process of work are also summarized in the appendices to provide more information on the learnings from the project.

2.0 Aluminum to steel resistance spot welds

Aluminum to steel resistance spot welding was performed using a medium frequency direct current (MFDC) welding machine designed for spot welding of aluminum alloys. The system used an inverter weld control from WTC (Welding Technology Corp, Farmington Hills, MI,) with MFDC transformers (RoMan Manuf., Grand Rapids, MI). Pneumatic actuators were used to apply weld force. Distilled water at ambient temperature was used to cool the welding electrodes at a flow rate of 1.5 to 2.0 gallons per minute. All welds were performed with the same CuZr C15000 copper alloy electrodes. GM's patented Multi-Ring Domed (MRD) electrode [2] was used on both the positive and negative welding electrodes. All welds were performed with the aluminum alloy sheet contacting the positive electrode [3].

Figure 1 shows a typical cross-sectional view of an aluminum to steel spot welded joint. In the figure, ridged surfaces are observed on the top and bottom of the weld zone due to the use of MRD electrode on both the aluminum and steel sheets, whose geometry includes ridges. A weld nugget appears to have formed in a thin trapezoidal shape only in the aluminum sheet whereas only a heat affected zone (no melting) is observed in the steel sheet.

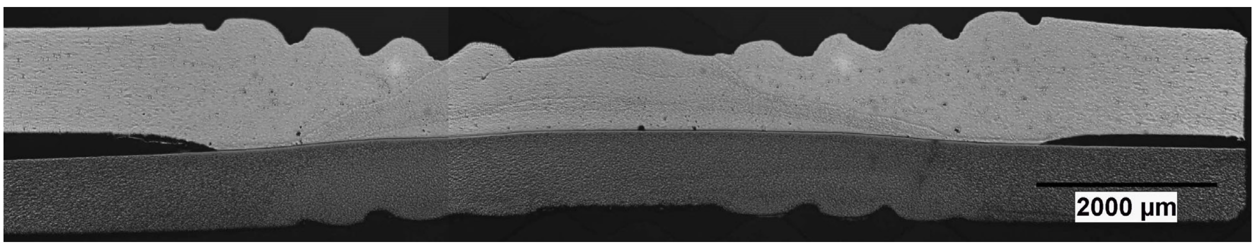

Figure 1. Cross-sectional view of a representative Al-steel spot welding. (Top: Aluminum, Bottom: steel)

2.1 Weld coupons and tests

For characterizing RSW joint performance, weld coupons for destructive testing were generated in three common test configurations used in the automotive industry. These include the coach peel, cross tension and lap shear tensile testing. The detailed coupon geometries and dimensions are presented in Figure 2.

Welding of several different material combinations was performed to make various joint microstructures that can cover a wide range of joint performance. Five weld joint configurations that are most relevant to GM's needs were studied by choosing a 1.2 mm thick aluminum alloy AA6022 and three hot dipped galvanized steel alloys (i.e., HSLA, LCS, CR210) in three different thicknesses (i.e., 0.9, 1.2, 2.0 mm). Post-heat treatment at 175°C for approximately 30 minutes was also applied to some weld coupons in order to examine the baking effects on the performance of aluminum to steel RSW joint. Note that this heat treatment is intended to mimic the automotive paint baking process. Hence, weld coupons with five different material combinations and three different baking conditions (i.e., 0BK, 1BK, 2BK) were generated.

Destructive tensile testing was first performed for all the conditions of interest (i.e., coupon geometries, material combinations and baking conditions). Seven coupons were tested for each condition to examine its repeatability. Out of the various mechanical performance data (e.g., peak load, energy absorption, retained button size etc.) obtained from the tests, the load-extension curves that are of the most interest are presented in Figure 34 in Appendix A. Note that the observed failure modes (BP or FT) of the seven coupons are also included in each plot. As shown in the figure, interfacial failure mode generally results in significantly lower peak load and/or rapid load drop which is unacceptable from the perspective of energy absorption capability. It is also of interest to see the difference in the peak load for different material combinations as well as for different baking conditions while the same aluminum sheet is used for all five material combinations and the failure always occurs in the aluminum sheet. This indicates that the joint performance can depend on the steel alloy/thickness welded to the aluminum as well as baking conditions.

Samples for microstructure and local property characterization were also prepared by cutting, mounting, and then polishing the mid cross-section of the joints. Microhardness measurements were performed for all the welding conditions, spanning across the aluminum and steel base material, heat affected zone (HAZ) and nugget. The local property change for different material combinations and baking conditions can be evaluated from these measurements. It is noted here that, to account for property variation across the joints, a linearly proportional relationship cany be assumed between the hardness and strengths (e.g., yield strength, ultimate tensile strengths) for aluminum and steel. Three samples were tested for each condition to examine its repeatability. The images of cross-sections after the hardness test and the hardness data across the nugget are presented in Figure 35 in Appendix B. In the figure, the red arrows point to the hardness data at the specific local locations. The two arrows in the left and right point to the boundaries between the base materials and the HAZ in steel, and the nugget in aluminum, respectively. The arrow in the center points to the first aluminum hardness data near the nugget center. It is observed in steel sheets that the hardness values increase from a low value in base material regions to higher values within the HAZ, and then decrease back to the lower value toward the interface region. In the aluminum sheet, the hardness values within the nugget regions are observed to be a little lower compared to those in the base material regions. It is noted from the figure that the hardness values in aluminum base material regions noticeably increase with the application of baking process, which is called as 'bake-hardening', whereas the hardness increase in other local regions in aluminum and steel appears to be insignificant.

It was reported [3] that thickness of the intermetallic compound (IMC) layer could have significant effect on the interfacial bond strength of aluminum to steel RSW joints and that thin layers result in higher bonding strength than thicker ones. In this work, IMC layer thicknesses were measured along the interface line of the weld for all the material combinations and baking conditions. Three samples were tested for each condition. The measured IMC layer thickness are presented in Figure 36 in Appendix C. In the figure, the numbers on the right side represent the average thickness of the IMC layers for each material combination, and the average thickness generally becomes larger for the material combinations with thicker steel sheets. It is observed that the IMC layer thickness appears not to change as a result of the baking process and it varies along the interface, having a minimum value near the weld outer edge and a maximum value at the weld center.

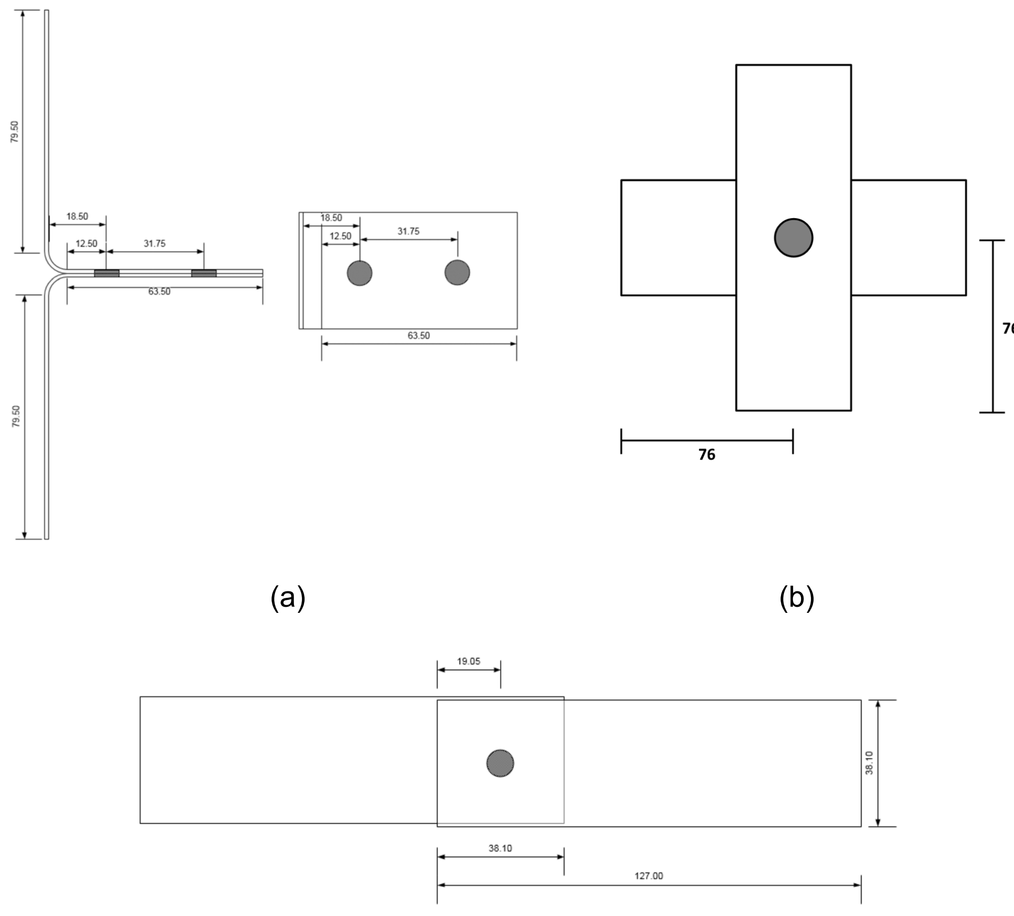

Figure 2. Geometry of weld coupons prepared for mechanical test. (a) Coach peel, (b) cross tension and (c) lap shear

2.2 Failure modes of welds

Resulting from the tensile testing, two primary failure modes are observed from the aluminum to steel RSW joints, button pull-out (BP) failure mode and interfacial failure (IF) mode. In BP failure mode, the fracture occurs in the aluminum material typically along/near the circumference of weld nugget due to higher bonding strength at the IMC layer, and the weld nugget remains on the steel sheet after failure, resulting in large fracture energy absorption. However, in IF failure mode, the interface layer rapidly separates at significantly lower load level, leading to very low energy absorption. Figure 3 shows some examples of failure modes that were observed from the post-weld mechanical testing. As shown in the figure, it is found that, for some cases, a half or partial button (i.e., HB/PB failure modes) may remain on the steel sheet after the failure. Even for these HB/PB failure modes, the fracture energy absorption is still expected to be quite substantial compared to IF failure mode, due to the occurrence of cracking in the aluminum material. Note that the IF failure mode is also known as face tear (FT) failure mode.

Failure Mode	Description	Picture
Full Button (B)	Approximately 75-100% of a round button is present	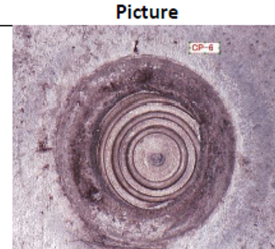
Half Button (HB)	Approximately 50% of a button is present	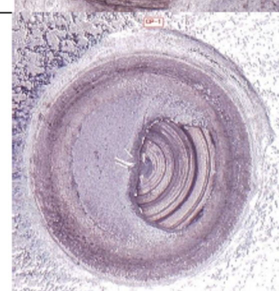
Partial Button (PB)	Less than 50% of a button is present	
Interfacial Tear AKA "Face Tear" (IF, FT)	No weld button is present	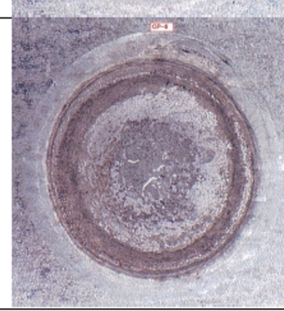

Figure 3. Example of failure modes in aluminum to steel resistant spot welding joints

Prior to initiating this project, the key factors influencing on the failure modes of aluminum to steel RSW joint were not understood. To help develop an understanding on these factors, one primary objective of the current project is to develop a modeling method that can predict the failure mode of this dissimilar material joint. For this purpose, failure modes of all the weld joints used in the destructive tensile testing were tracked in order to relate possible key factors, if any, influencing on the failure modes. For some welding conditions, HB/PB failure modes are also observed. In this work, HB/PB modes are categorized into BP mode as aluminum fracture appears to be key contributor to their energy absorption.

Based on this categorization, the failure modes for all the joints are listed in Table 1. Note that seven coupons were tested for each condition and, for some conditions, both BP (B) and IF (FT) failure modes were observed without clear predominance. As shown in the table, the fracture modes may be different for different material combinations even before the baking process (Compare, for example, CT/No Bake (0BK) samples for E120 and E141). Also, the fracture mode may change with the application of baking process (Compare, for example, CP/E141 samples for 0BK and twice baked (2BK)).

One material combination was planned to be selected for developing/tuning finite element modeling method for weld joint simulations. Note that a combination is preferred that shows clearer predominance of a failure mode in different baking conditions. E141 combination is selected for this purpose as it tends to show BP and IF modes in CP/LS/0BK and CP/LS/2BK, respectively, whereas its CT coupons tends to show IF modes regardless of baking condition.

Table 1. Observed failure modes for different coupon geometries, baking conditions and material combinations. (Here, the numbers in the table represent the number of samples (out of seven) showing the corresponding failure mode)

Comb.#	**1.2mm 6022 Al**	**CP**			**CT**			**LS**		
		0BK	1BK	2BK	0BK	1BK	2BK	0BK	1BK	2BK
E120	1.2mm HDG HSLA	7B	7B	7B	7B	7B	7B	3B 4FT	6B 1FT	7B
E141	0.9mm HDG HSLA	7B	7B	7FT	1B 6FT	2B 5FT	2B 5FT	5B 2FT	6B 1FT	2B 5FT
E133	2mm HDG LCS	7B	7B	7B	5B 2FT	7B	6B 1FT	7FT	5B 2FT	4B 3FT
E135	1.2mm HDG LCS	7B	7B	7FT	4B 3FT	3B 4FT	2B 5FT	1B 6FT	4B 3FT	4B 3FT
E129	1.2mm HDG CR210b2	7B	7B	7B	5B 2FT	6B 1FT	7B	7FT	3B 4FT	3B 4FT

3.0 Characterization of weld nugget properties

It was anticipated that microstructure information and local material properties at a fine resolution would be required as inputs to the FE model to enable more accurate model output and prediction of failure modes. Specimens were prepared and characterized for microstructures and local properties using various analysis tools. Light microscopy was used to elucidate the nugget, HAZ, and base metal regions within the joint. Thickness of the Fe-Al IMC was measured from light microscopy using image analysis algorithms or by scanning electron microscope (SEM), depending on the thickness of the IMC (See Appendix C). This morphology information can be provided for generating more accurate solid model. Energy dispersive spectroscopy (EDS) was employed to determine the composition of the IMC, and electron backscatter diffraction (EBSD) was used to quantify grain size distribution and to differentiate between IMC phases. Nano-indentation was performed for extracting the local stress-strain relations within the weld nugget regions.

In this section, some key results as well as the lessons learned from the characterization work are reported that are directly used as the input information for the FE models.

3.1 Microstructure and hardness map

As mentioned in the previous section, a weld nugget shaped in a thin trapezoid can be seen in the aluminum sheet whereas an elliptical HAZ can be seen in the steel sheet. SEM was adopted to examine the microstructures within the weld nugget regions. Figure 3(a) shows the combined SEM image for the weld nugget region. As shown in the figure, a trapezoidal-shaped weld nugget can be clearly seen in the aluminum sheet, which is due to the different microstructures between the base material region and weld nugget region. The weld nugget contains material that was melted and resolidified after joining. It is noted that the grains within the Al weld nugget are highly elongated across the whole region, compared to small equibiaxial-shaped grains in the base material region. In the steel sheet, much finer grains can be seen within the HAZ compared to relatively large-sized grains in the base material region. Figure 4(b) is an example image showing IMC layer structure near nugget center. In this image, needle-like steel remnant is not observed in IMC layer. The IMC thickness seems to be quite thin (i.e., 1~2 μm) and the thickness is rather consistent along the length direction.

While the microstructure within Al weld nugget appears to be consistent across the region as shown in (a), the cross-sectional images in Figure 1 and Figure 35 show possible existence of 2~3 different thin layers (or zones) within the Al weld nugget (especially in E141 samples). In order to examine the existence of different zones, hardness testing was performed across the weld nugget as shown in Figure 5(a). The resulting topographical micro-hardness map is presented in Figure 5(b). As shown in the figure, there seem to be 2~3 zones with slightly different hardness values within the Al weld nugget. It is also noted that E141 samples in Figure 35 shows slight increase in hardness values across the Al weld nugget. As expected, hardness values are higher within the elliptical-shaped HAZ in steel sheet. The information based on this hardness map is adopted in generating the FE models for weld joints.

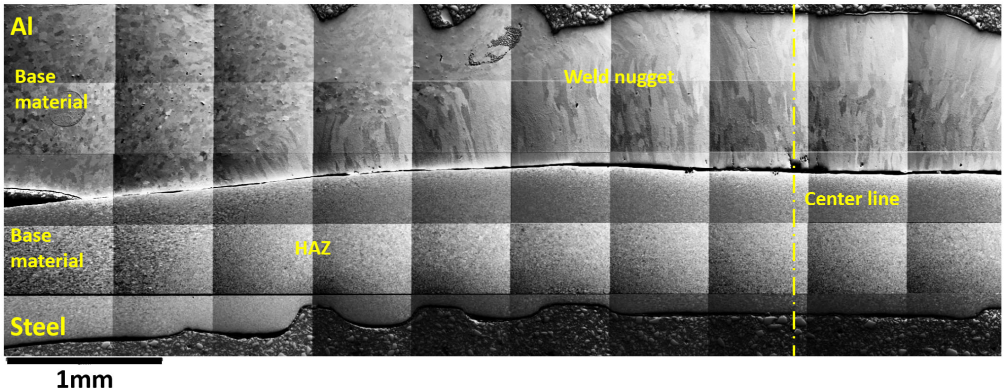

(a)

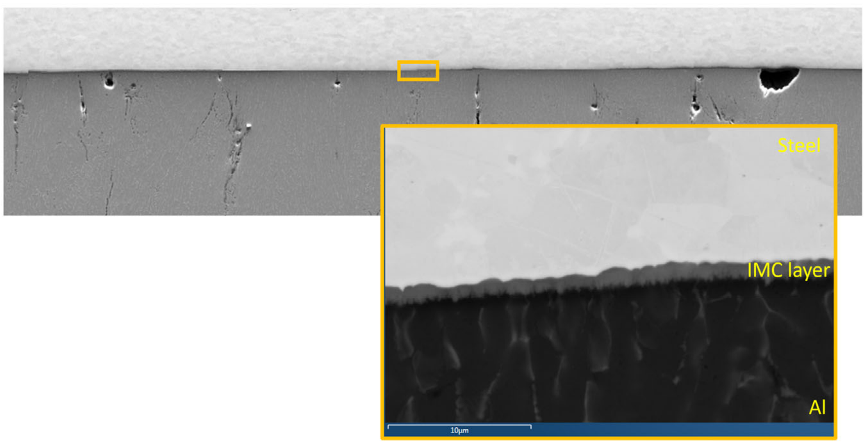

(b)

Figure 4. (a) Metal microstructures in weld nugget and (b) IMC layer near nugget center.

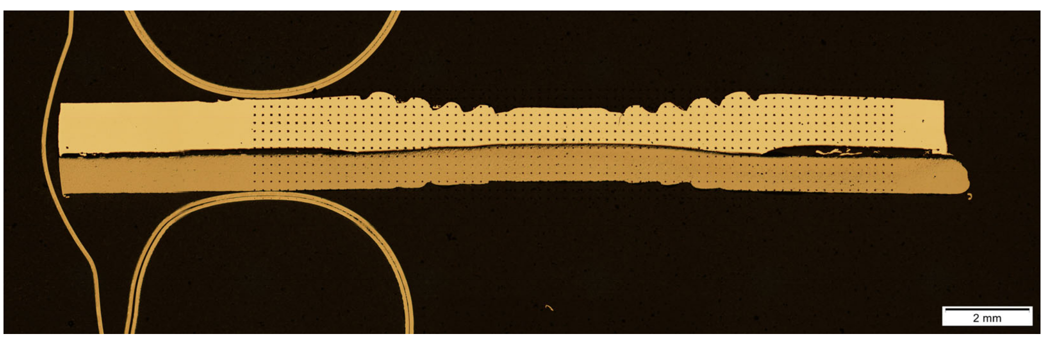

(a)

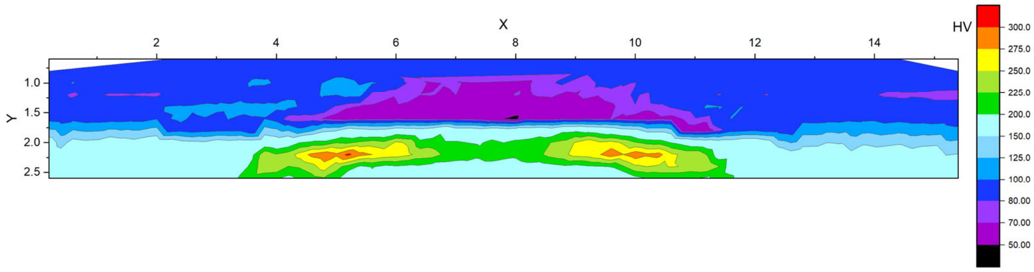

(b)

Figure 5. (a) Cross-sectional view of a weld nugget after microhardness measurement and (b) topographical hardness map.

3.2 Application of nano-indentation for property estimation

Nano-indentation tests were initially performed using a Nanovea nano-hardness tester shown in Figure 6(a) with a Berkovich indenter for extracting the local stress-strain relations of aluminum and steel within the weld nugget regions as wells as of IMC layer. For IMC layer, however, meaningful experimental data could not be obtained with the currently available indenter tip and the load-controlled tester due to very thin thickness of the layer versus the size of indenter tip. Note that enough indent spacing (>3 times indent size) is required to avoid the effects from neighboring indents and/or dissimilar materials.

Nano-indentation tests were therefore performed for the purpose of extracting the properties of aluminum and steel. The tests were first performed on the base material regions to validate the testing/extractions methods against tensile stress-strain curves of base materials. For example, Figure 6(b) shows a microscopic image of aluminum base material region after the indentation test. Twelve indents with 80 μm spacing were done to obtain the average material response.

Figure 7 shows the load-depth curves obtained from the test for aluminum and steel base material regions of E141 material combination. In general, the obtained curves have typical and smooth shapes that are expected from Berkovich indenter. However, for many curves, the load increase begins after some indentation depth (e.g., 0.5~1 μm), which is not a typical phenomenon. There may be a few reasons for this issue: surface roughness, oxidation or machine misalignment etc. A significant effort was initiated to determine the source of this issue and resolve it. During this period, the team attempted to extract the stress-strain curves based on the currently obtained load-depth curves shown in Figure 7.

Figure 8(a) shows the schematics of Berkovich indentation, load-depth curve and power-law elastic-plastic material response. The power law material response is represented by the equations included in the figure. Note that the elastic modulus E, yield strength σ_y and hardening exponent n are to be decided for a complete equation. Figure 8(b) shows an inverse algorithm used for extracting stress-strain curves from nano-indentation tests. This method was suggested by Cheng et al. [4] by combining the Dao's method [5] and an empirical yield strength-hardness relation, and was demonstrated to be appropriate for estimating the stress-strain curves of ferrite and martensite phases of dual phase steels.

As the indentation depth has significant effects on the stress-strain curve estimation, the resulting stress-strain curves will depend on how to manage the initial zero-loading depth of 0.5~1 μm. Various methods/assumptions for managing the initial portion of the load-depth curves were investigated in an effort to obtain stress-strain curves that reasonably match with the experimental tensile curves. Figure 9 shows the comparison of the estimated stress-strain curves with the experimental curves for aluminum and steel. In each plot, the red-colored curve was determined by averaging the multiple stress-strain curves obtained from each indentation. As shown in the figure, the average curves generally show the strength level similar to those of experimental curves; however, the hardening rates do not match well with the experiments. It was anticipated that more accurate stress-strain curves would be required in this modeling work for better predicting different failure behaviors resulting from only a slight difference in material parameters. Thus, the current indentation approach using Berkovich indenter appeared not to be suitable for extracting the accurate local stress-stain curves.

A spherical shaped indenter was also explored towards extracting the stress-strain curves. Indentation test were performed using Nanovea tester, and several load-depth curves were obtained from aluminum and steel base material regions. Two methods (i.e., Tabor's method

[6], Cao and Lu method [7]) were adopted in estimating the stress-strain curves. Figure 37 and Figure 38 in Appendix D show the comparison of stress-strain curves estimated from spherical indentation test with experiments for aluminum and steel based on Tabor's method [6] and Cao and Lu Method [7], respectively. As shown in the figures, results matching with experimental data were not obtained, and the discrepancy between the estimated curves and experimental ones is even larger than those of results based on Berkovich indenter. This suggests that using spherical indenters is also not a suitable method for estimating stress-strain curves.

The feasibility of using a finite element modeling method was also explored as an approach to back-estimate the material's stress-strain curves from load-depth curves. Two-dimensional (2D) axisymmetric and three-dimensional (3D) models were generated with different types of indenter tips (i.e., Berkovich tip, spherical tip and flat tip). Figure 39 in Appendix E shows some examples of the generated 3D models with different tips. For these models, experimentally obtained stress-strain curves in Figure 40(a) in Appendix E are used as the material input properties, and it is therefore expected that the resulting load-depth curves from simulations should match with the curves from indentation tests. Figure 40(a), Figure 40(b) and Figure 40(c) in Appendix E show the comparison of load-depth curves obtained from simulations with experimental ones for the different tips. In the figures, contrary to the expectation, the curves from the simulations do not match well with the experimental ones. Various simulation options (e.g., friction coefficient, mesh size, indenter tip angle etc.) were tested to examine their effects on the load-depth curves. From these simulations, it was found that the tested options do not have quite noticeable effects on the load-depth curves, and well-matched results could not be obtained between simulations and experiments. This indicates that the FE modeling method may not be a feasible way for extracting the accurate stress-strain curves. Nevertheless, it appeared to be a better method compared to the indentation method.

As presented above, some methods and approaches (e.g., FEM, Berkovich indenter) resulted in somewhat better accuracy than others, but no single method resulted in a universal solution with accuracy level acceptable for the objective of this task. It appears that the recommended methods in the published literature were developed based on different-sized/shaped tips for different materials, therefore may be applied to rather specific material systems and/or testing methods. It was concluded that nano-hardness test method and FEM method could not be used for the objective of project.

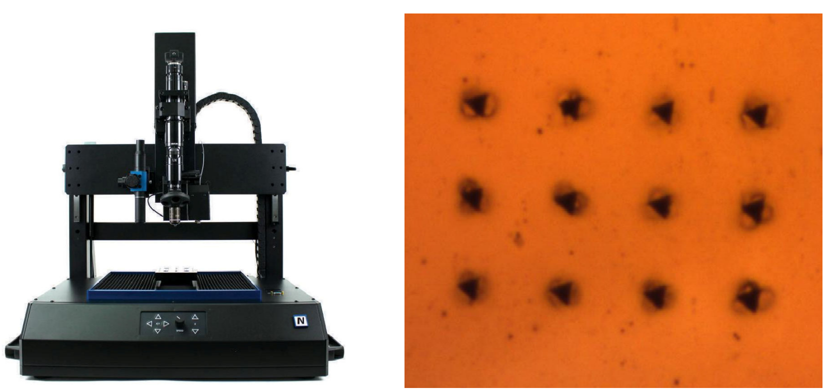

(a) (b)

Figure 6. (a) Nanovea nano-hardness tester and (b) microscopic image of aluminum base material region after nano-indentation test (80µm indent spacing).

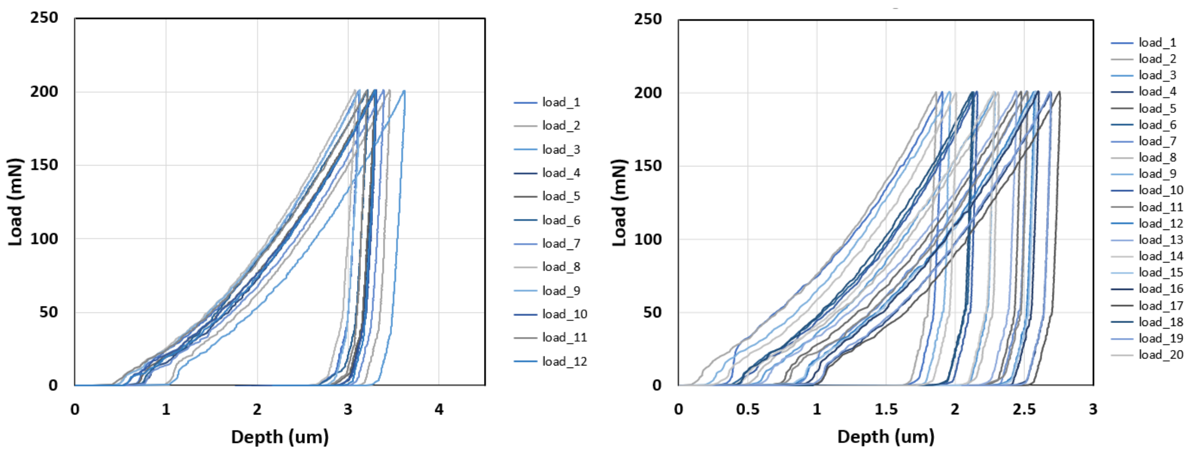

(a) (b)

Figure 7. Load-depth curves obtained from nano-indentation tests for (a) aluminum and (b) steel base material regions of material combination E141.

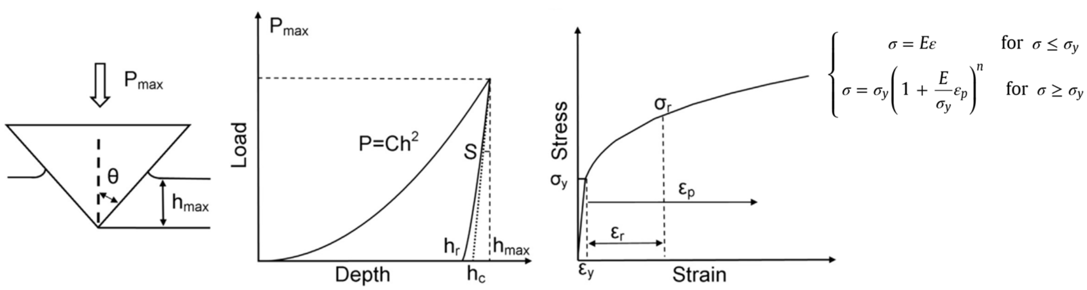

(a)

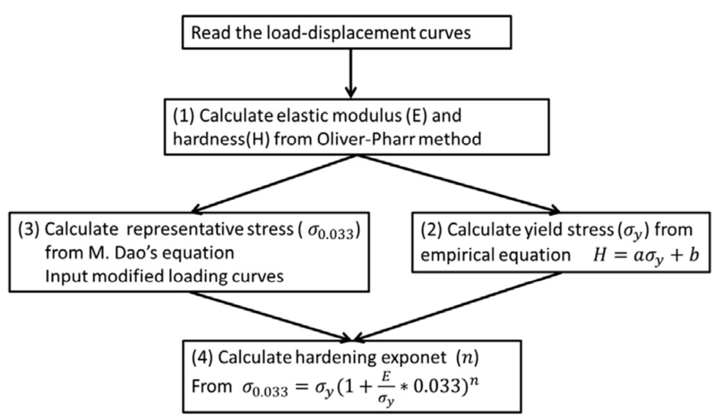

(b)

Figure 8. (a) Schematics of Berkovich indentation, load-depth curve and power-law elastic-plastic material response and (b) inverse calculation algorithm to estimate the elastic-plastic properties from indentation load-depth curve [4].

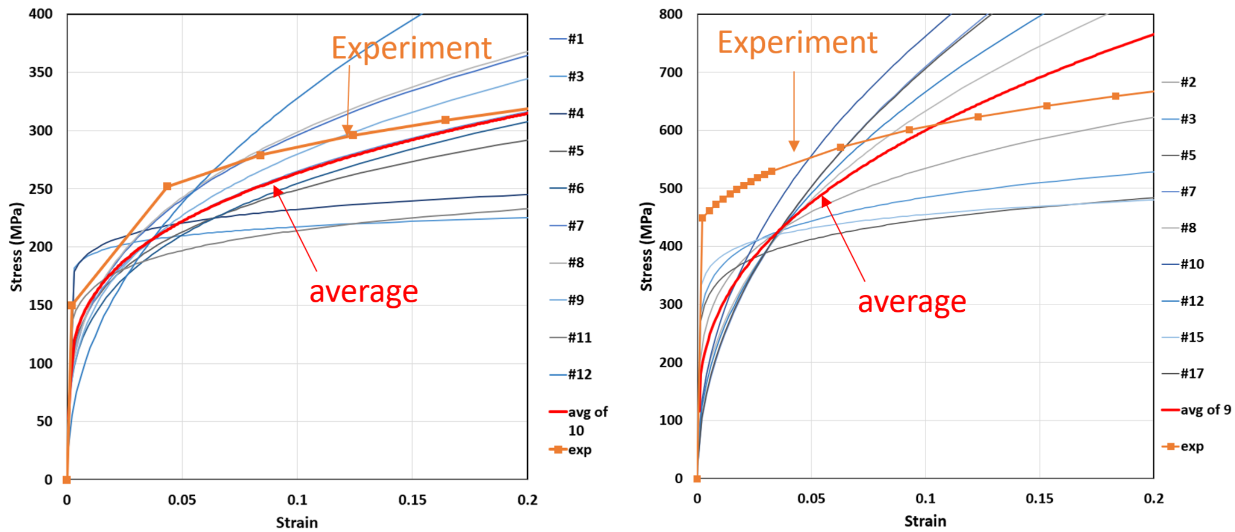

(a) (b)

Figure 9. Comparison of stress-strain curves estimated from Berkovich nano-indentation tests with experiments for (a) aluminum and (b) steel.

3.3 Use of microhardness data for property estimation

As mentioned in the previous section, the use of load-displacement curves from nano-indentation testing for extracting the stress-strain curves did not provide sufficient accuracy. An alternate method was devised based on the microhardness data obtained from the weld coupons shown in Figure 10(a). In this method, the material properties near the extremities of the measurement line (i.e., red-dotted box and blue-dotted box in the figure) are not affected during the welding process as these locations are away from the weld nugget. Additionally, they are assumed to have the same properties as those of base materials.

As part of the material characterization efforts, standard tensile tests were also performed with all of the selected base materials (i.e., one aluminum sheet and five different steel sheets listed in Table 1 for different baking conditions (i.e., 0BK, 1BK, 2BK). For example, Figure 10(b) and Figure 10(c) show the obtained stress-strain curves of aluminum and some steels, respectively, for different baking conditions. Note that, for aluminum, the tensile tests were performed along the rolling and transverse directions. As shown in the figures, significant bake-hardening occurs in aluminum sheet whereas the hardening effects in the steel sheets are insignificant.

In this alternate method for determining local material properties, all the tensile curves are first approximated by the power-law relation using the data beyond the strain level of ~5% as shown in Figure 10(b) and Figure 10(c). The yield strength and ultimate tensile strength (UTS) were determined from each power-law curve by finding the intersection point between the elasticity line and the power-law curve and by assuming the UTS occurs at the same strain level as the hardening exponent. The yield strength and UTS determined this way are then plotted with hardness values of the base material regions, and the linear relationship was assumed between strength and hardness as shown in Figure 11.

The obtained linear relationship was then used to back-estimate the stress-strain curves based on given micro-hardness values. Figure 12 shows the comparison of stress-strain curves back-estimated based on hardness-strength relationship with experimental curves for aluminum and steels. As shown in the figure, the estimated curves are generally well-matched with the experimental curves except for the initial yield regions. As large plastic deformation and fracture are of interest in this modeling, the discrepancy in the initial yielding regions is not expected to have meaningful effects on the final results. It was decided in this project that the alternate method suggested here was to be used to estimate the local material properties within the weld nugget.

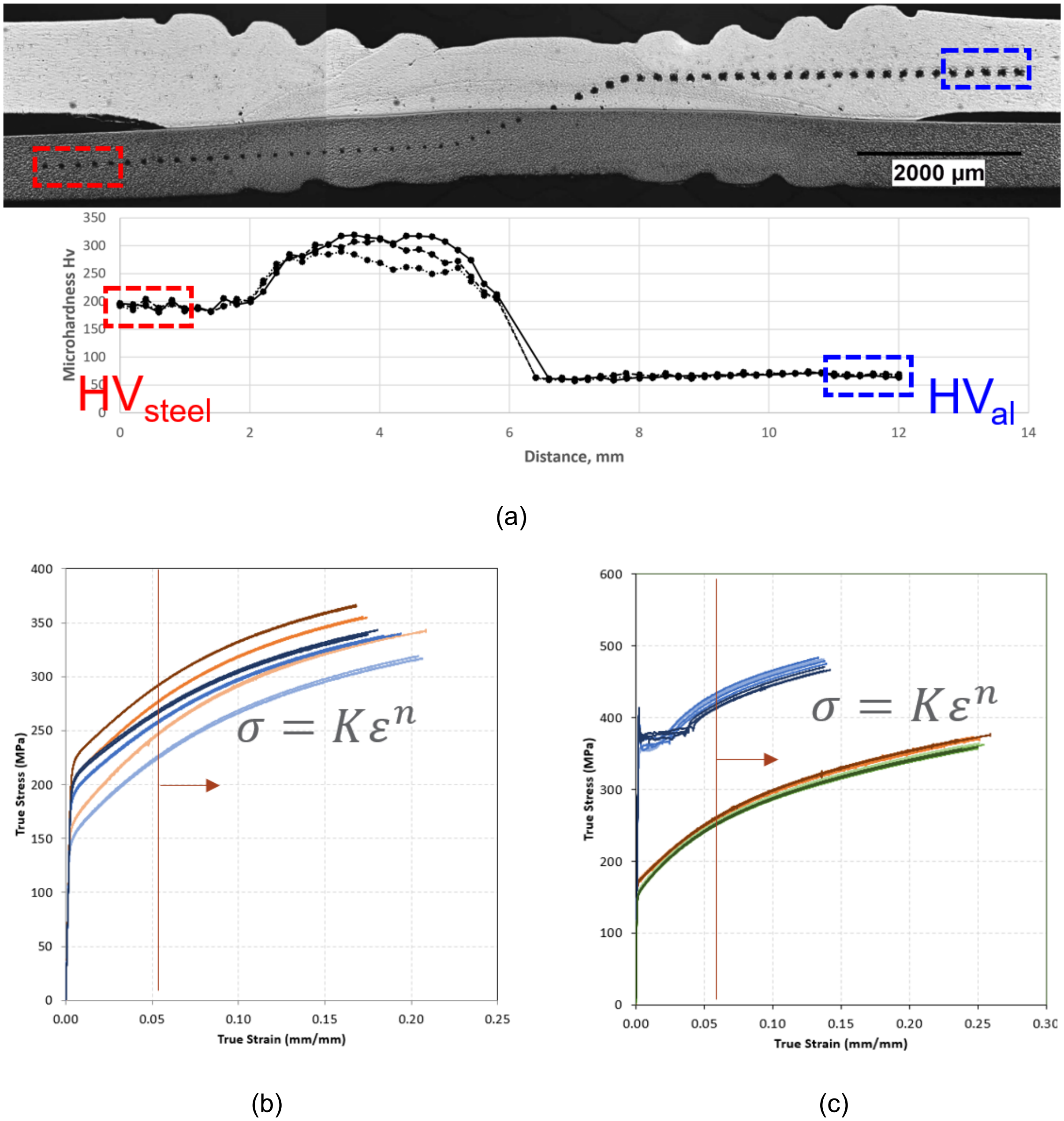

Figure 10. (a) Microhardness measurements across the weld nugget regions and selection of hardness data from base material regions, (b) tension stress-strain curves of aluminum for different directions and baking conditions and (c) tensile stress-strain curves for various steels for different baking conditions.

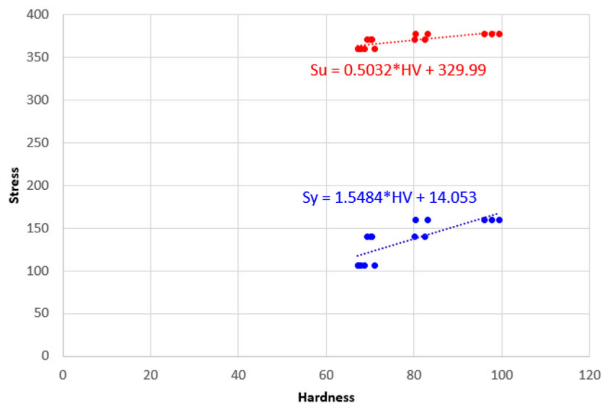

(a)

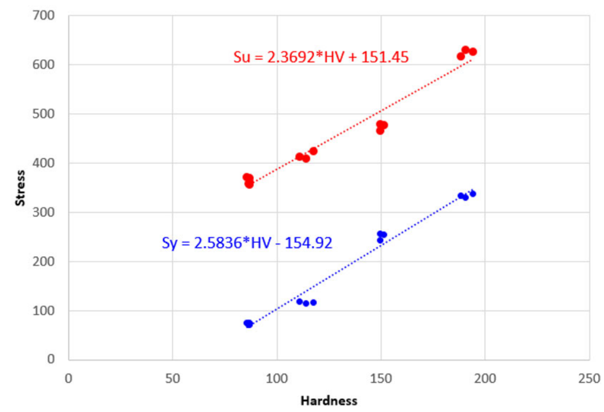

(b)

Figure 11. Relationship between hardness and strength for (a) aluminum and (b) steel.

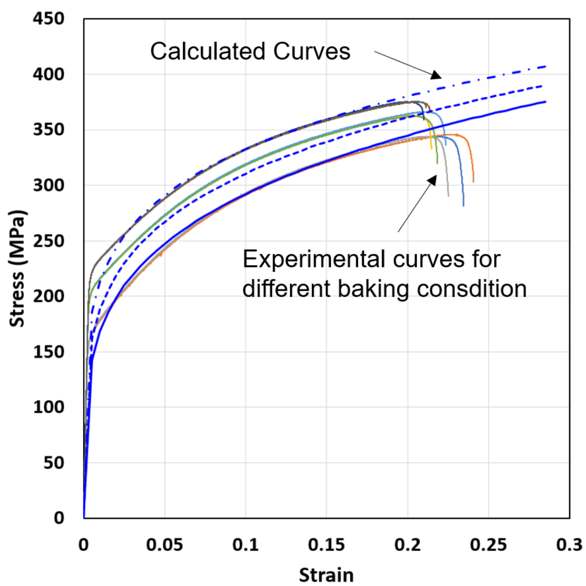

(a)

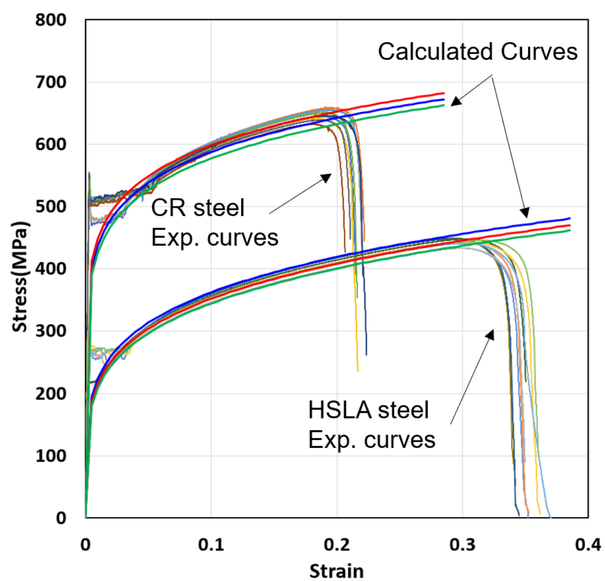

(b)

Figure 12. Comparison of stress-strain curves estimated based on hardness-strength relationship with experimental curves for (a) aluminum and (b) steel.

4.0 Finite element model

Overall geometries of finite element models for coach peel, cross tension and lap shear samples are presented in Figure 13. Due to the symmetry of the coupons, only the half of coupon geometries were modeled in an effort to reduce simulation time. Note that the coach peel coupon has two identical welds with the distance of ~32mm. However, for coach peel coupons, the tensile test is halted right after the first weld fails. Therefore, the second weld is modeled using simple flat geometry.

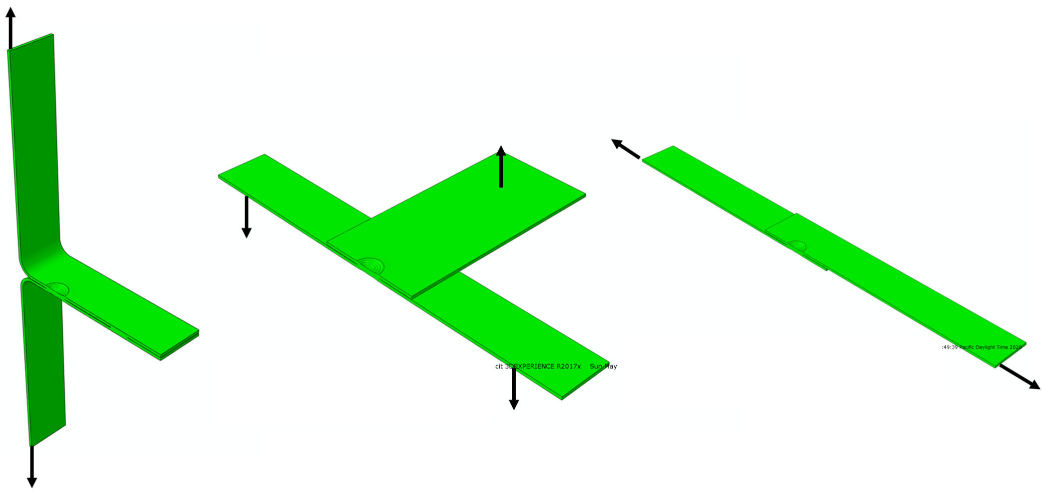

(a) (b) (c)

Figure 13. Finite element model geometry for (a) coach peel sample, (b) cross tension sample and (c) lap shear sample.

4.1 Weld nugget model and property assignment

The finite element model for weld nugget region was generated based on the actual weld geometry presented in the previous sections. Figure 14 shows the generated weld nugget model, cross-sectional view and the meshed IMC layer. Eight-node reduced integration linear brick elements (C3D8R : Continuum 3-Dimensional 8-node element with Reduced integration point) were used in the model, and finer meshes were adopted near the edge of the weld nugget and joint interface. In the figure, the different-colored zones represent the different element sets which were grouped based on the observations of microstructures in Figure 4, hardness map in Figure 5 and microhardness test results in Figure 35. As discussed previously, the trapezoidal-shaped Al weld nugget region was divided into three thin-layered zones, and the steel sheet was modeled to have two different HAZ.

The IMC layer was modeled using solid elements (C3D8R) with consideration of thickness variation from the nugget center to the edge. Note that the bonding strength of IMC layer may depend on the thickness. Therefore, IMC layer was also modeled to have different zones as shown in the figure to consider the potential strength variation along the radial direction. Cohesive surface (or element) may have been used to model the IMC interlayer failure behavior. However, it was learned from previous project efforts that two or more material parameters are needed for the cohesive elements to be correctly used for modeling of the bonding/fracture behavior. For simplicity, in this work, solid elements were used for the IMC layer, and the stress-based brittle fracture criteria with a single material parameter were adopted to describe the fracture of IMC layer.

Figure 15(a) and Figure 15(b) show the hardness values assigned to different zones of the FE models for 0BK and 2BK conditions. These values are from the microhardness tests for E141 material combination shown in Figure 15. Relatively large bake-hardening effects can be seen for the aluminum sheet. These assigned hardness values were used to estimate the stress-strain curves for the different zones. Figure 15(c) shows the examples of stress-strain curves of aluminum and steel estimated based on the assgined hardness values for E141. With the stress-strain input data determined for the model, fracture criteria for the three materials (i.e., aluminum, steel, IMC layer) also need to be determined.

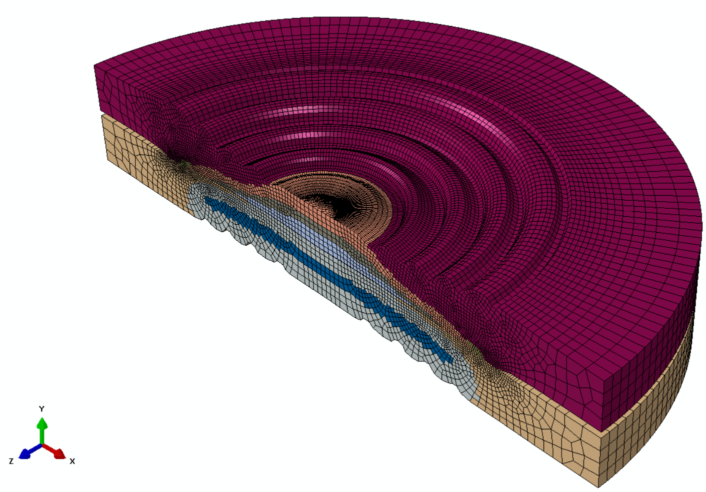

(a)

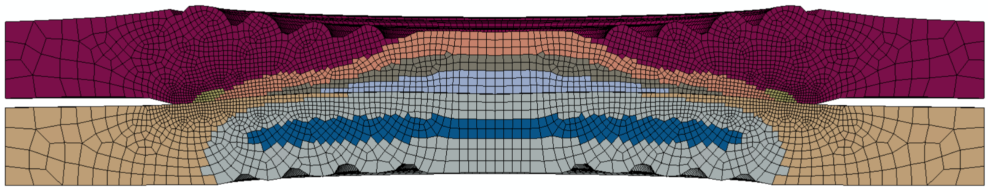

(b)

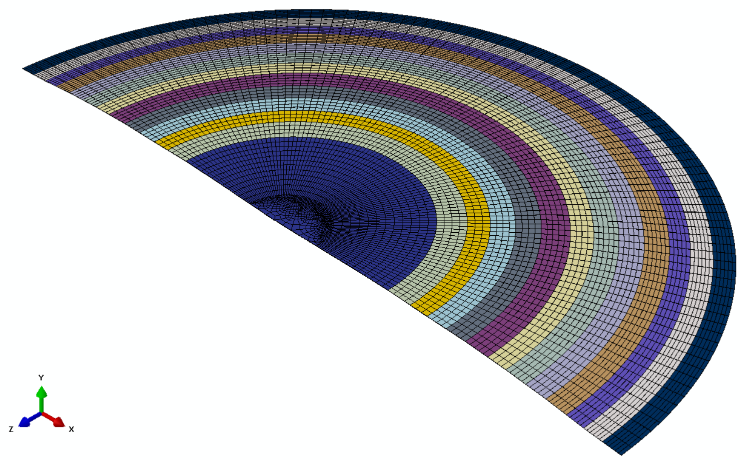

(c)

Figure 14. (a) Finite element model of weld nugget region, (b) side view of cross-section and (c) model of IMC layer. Different colors represent the different element sets grouped based on microscopic images of cross-sections and hardenss map.

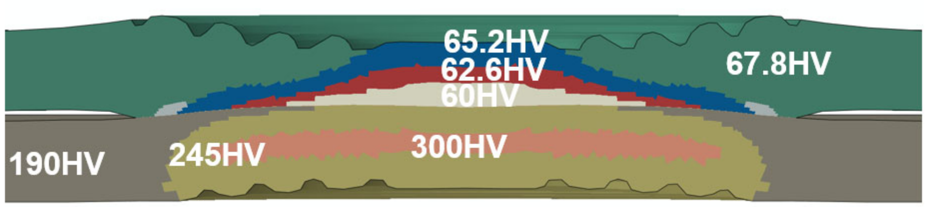

(a)

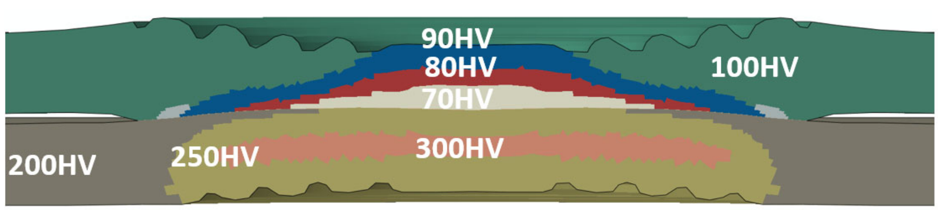

(b)

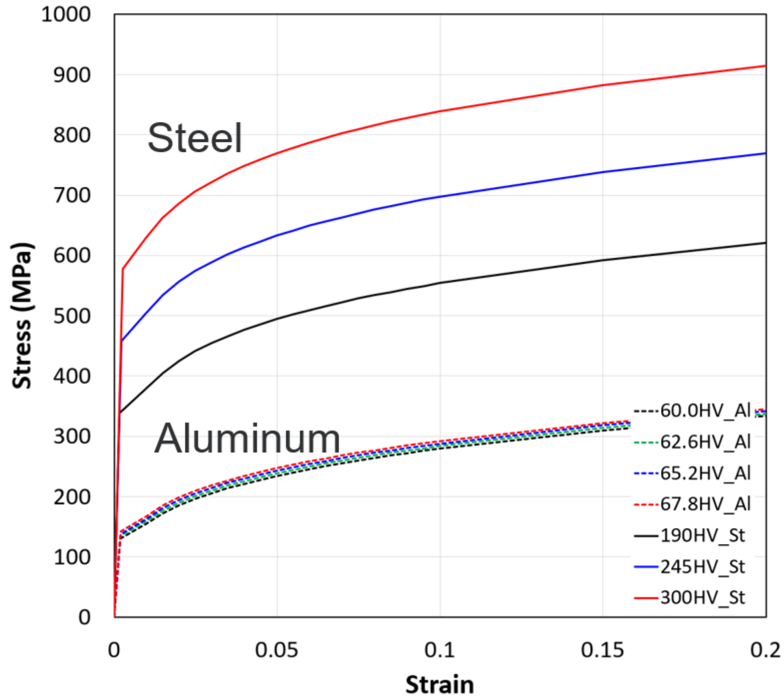

(c)

Figure 15. Hardness value assignment within the weld nugget region and base material regions for (a) 0BK and (b) 2BK conditions and (c) examples of stress-strain curves of aluminum and steel estimated for differnet hardness values.

4.2 Estimation of fracture strain curve for aluminum

For the weld nugget failure simulations, the fracture criteria need to be established for the materials in the FE model. It was observed that the steel sheets never fail during the destructive tensile test of weld coupons whereas the aluminum sheet cracks/tears or IMC layer separates as discussed in the previous sections. Thus, no fracture criterion is adopted for the steel sheets in this modeling work.

In general, strain-based damage model is adopted for ductile materials while stress-based damage model is used for brittle materials. Hence, for the aluminum sheet here, a strain-based ductile damage model was adopted for the failure modeling, where the accumulated equivalent plastic strain is used for calculating the damage-level. With the damage model adopted, the element whose accumulated equivalent plastic strain reaches a specified critical value is removed from the model, which eventually leads to the fracture of the model. In this ductile damage model, this critical value is defined as the fracture strain. One of the difficulties in estimating the fracture strain is that it depends on the element/mesh size adopted in the model. For this reason, tensile models were generated using the elements that have the same size as those near the edge of weld nugget region at the interface of the aluminum and steel. Then, tensile simulations were iteratively performed by adjusting the fracture strain level until the overall shape and fracture point of the simulated stress-strain curve matched well with those of the experimental curve. Figure 16 shows the simulated models under tensile loading and the comparison of simulated curves with experimental curves for 0BK and 2BK conditions. As shown in the figure, the simulated curves match well with the experimental curves for both the shape and the fracture point (i.e., blue-colored 'x'). This allowed the fracture strain levels under the tensile loading condtion to be accurately estimated for 0BK and 2BK conditons. Note that the fracture strains estimated here are for the base materials.

For the aluminum, the fracture strain often depends on the stress triaixaility as shown in Figure 17(a). The stress triaxiality (η) is definded as $\eta = -p/q$, where p is the pressure stress and q is the Mises equivalent stress. Note that the stress triaxiality for tensile loading is 0.33. Due to the unavailability of the stress triaxiality dependency of fracture strain for the aluminum (i.e., AA6022) at the early stage of modeling work, the initial approach was to adopt the fracture strain curve shown in Figure 17(a) [8] as the baseline curve, and scale the curve upwards or downwards as needed to adjust the fracture strain level.

With the obtained information (i.e., stress-strain curves, Al fracture strain level under tensile loading and stress triaxiality dependency of fracture strain curve for 0BK and 2BK conditions), a series of destructive tensile simulations were first performed for coach peel, cross tension and lap shear weld coupons. For this first trial of simulation, ABAQUS built-in stress-based fracture criterion (i.e., mean stress-based criterion : $\sigma_m > \sigma_{cr}$ where $\sigma_m = (\sigma_1 + \sigma_2 + \sigma_3)/3$) [9] was adopted for IMC layer, and the IMC fracture strength was assumed not to change from the baking process. Then, in the series of simulations, the Al fracture strain level was iteratively adjusted from the values estimated in tensile simulations (in Figure 16) until the failure modes predicted from various coupon model simulations generally matched with the experimentally observed modes for E141. Note here that the fracture strain level for lower hardness regions within the Al weld nugget was determined by scaling up the curve for the base materials according to the hardness difference.

The aluminum fracture strain curves estimated from these first coupon model simulaitons are presented in Figure 17(b) for the 0BK and 2BK base materials. It can be seen from the figure that 0BK aluminum has higher ductility compared to 2BK aluminum as its fracture strain level is higher. Note that the fracture strain levels for tensile loading (η =0.33) are ~110% and ~40% for 0BK and 2BK conditions, respectively, and these high values are based on the small element/mesh sizes near the crack tip of Al weld nugget. Next, the Al fracture strain curves presented in Figure 17(b) were to be used as the input data for the next series of coupon model tensile test simulations.

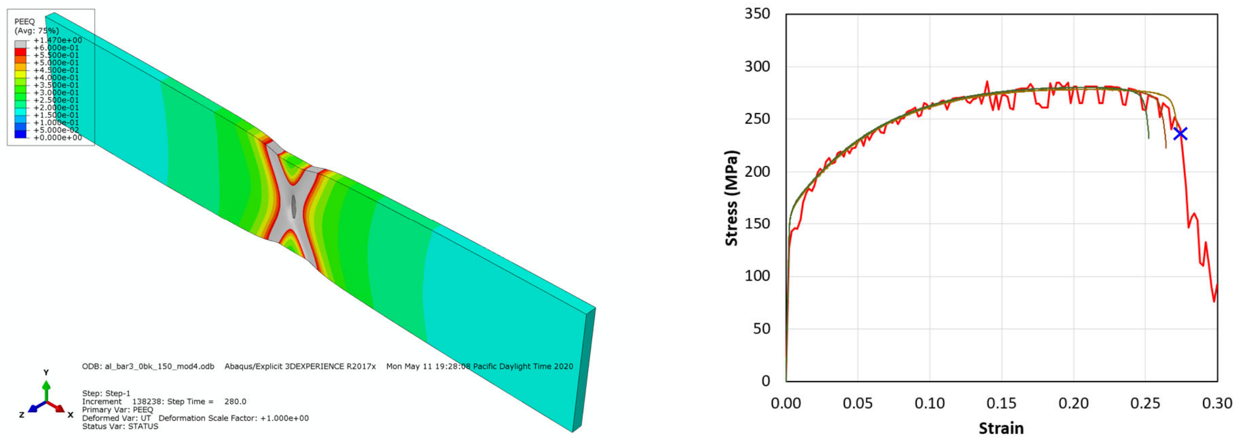

(a)

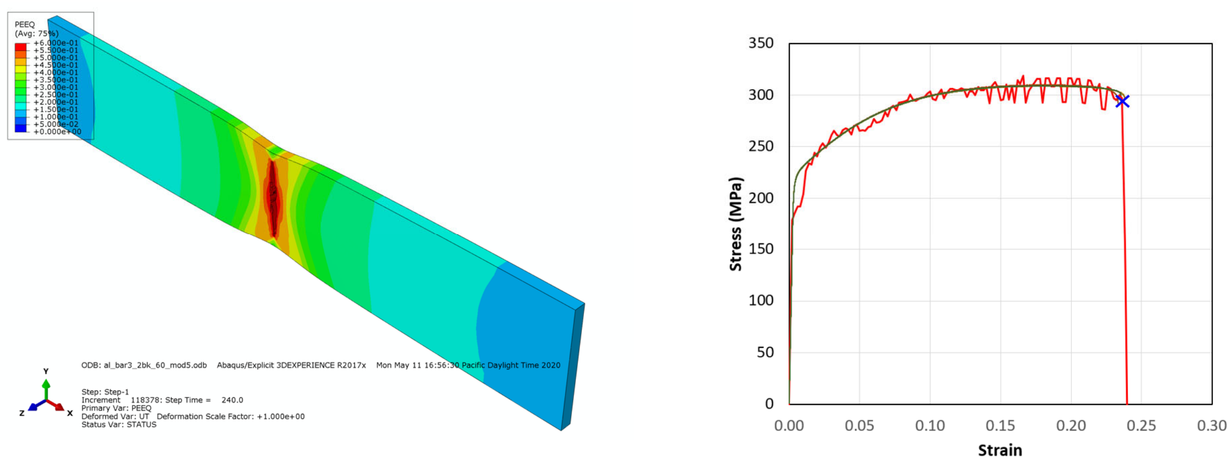

(b)

Figure 16. Simulation for estimating the fracture strain level under tension, and comparison of simulated curve with experimental one. (a) 0 baking and (b) 2 baking conditions.

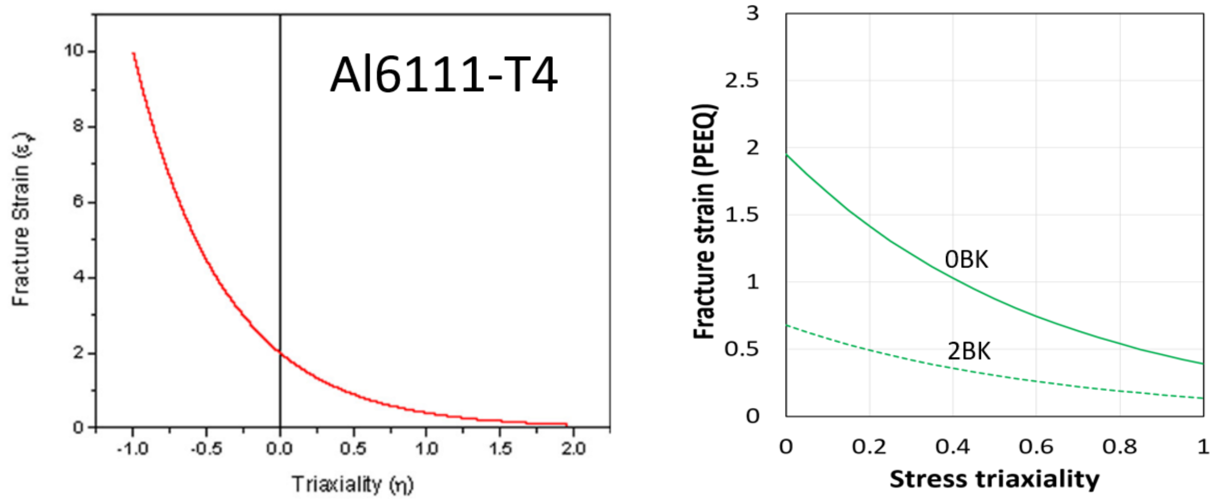

(a) (b)

Figure 17. (a) Example of stress triaxiality dependency of aluminum fracture strain curve and (b) aluminum fracture strain curves estimated/assumed based on tensile simulations for 0BK and 2BK aluminums.

4.3 Brittle fracture criterion for IMC layer

In this project, solid elements were chosen for the IMC layer, and the stress-based brittle fracture criteria with a single material parameter was employed to describe the fracture of IMC layer. Two different fracture criteria were tested in this work.

- The first criterion was an ABAQUS built-in fracture model which is referred to as the mean stress-based criterion as mentioned in the previous section. In this fracture criterion, the IMC element whose mean stress is higher than the given critical value ($\sigma_m > \sigma_{cr}$) is removed from the model. Note however that dominant fracture modes (e.g., normal fracture or shear fracture) cannot be differentiated using this fracture criterion.

- For the second criterion, the Griffith brittle fracture criterion [10] was adopted in order to diffrentiate the dominancy of one fracture mode of IMC layer. The goal of testng the Griffith criterion was to examine its applicability for capturing the shear dominant fracture mode of IMC layer, especailly, for LS samples. Due to the minute thickness of IMC layer, the Griffith criterion for biaxial stresses can be directly applied for the IMC fracture in the form of

$$\sigma_1 = \sigma_{ts} \qquad \text{if } 3\sigma_1 + \sigma_3 > 0$$

$$(\sigma_1 - \sigma_3)^2 + 8\sigma_{ts}(\sigma_1 + \sigma_3) = 0 \qquad \text{if } 3\sigma_1 + \sigma_3 < 0$$

where σ_1 and σ_3 are the maximum and minimum principal stresses, respectively, and σ_{ts} is the uniaixal tensile strength which can be the IMC fracture strength in this case. Figure 18 shows the two possible fracture modes predcted from the Griffith criterion and their corresponding regions in the σ_1-σ_3 stress space (see the quadrant IV in the figure). Note that a user-subroutine code was developed in order to implement this fracture criterion into the ABAQUS.

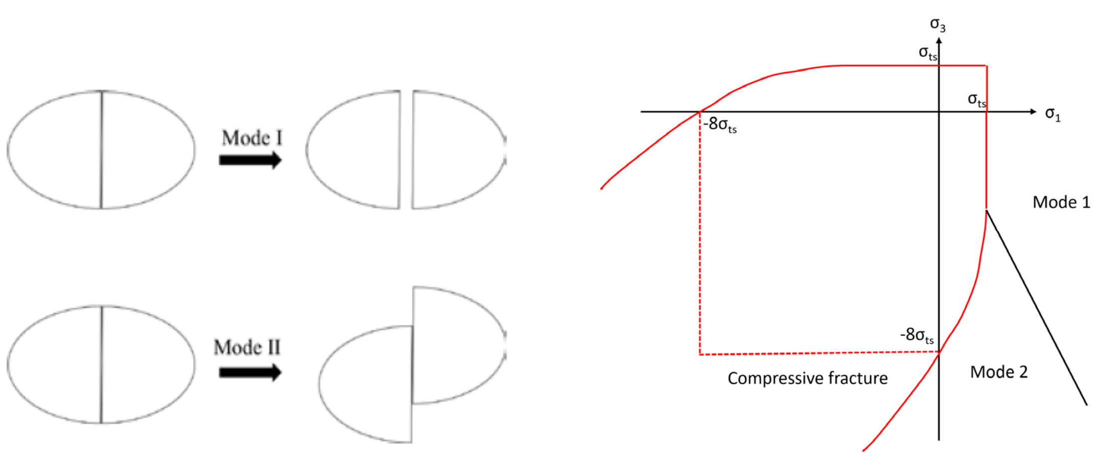

Figure 18. (a) Two fracture modes of Griffith brittle fracture criterion (normal/shear modes) and (b) stress fracture criterion contour in 2D stress space.

5.0 Computational approaches

The primary objectives of the project were to predict the failure modes of the weld coupons of different material combinations under various destructive test configurations (i.e., CP, CT and LS tests) and to develop an understanding of the key factors influencing on those different failure modes. In this study, the simulation tasks were first focused on the prediction of failure modes of six different coupon conditions (i.e., CP, CT, LS in 0BK and 2BK conditions) for the selected material combination E141 (Refer to Table 1 for details of the joint configurations) in order to have some initial understanding of the key influencing factors. Based on the observations obtained from the first simulation tasks, the next simulation tasks were set to capture both the fracture mode and load-extension curve for CP and LS samples as these two sample types are of more interest in engineering.

5.1 Failure mode prediction with various fracture criteria

Initially, simulation tasks were performed based on the material parameters for aluminum and steels and the IMC fracture criteria described in the previous sections. For the purpose of predicting the failure modes for the six sample conditions, different fracture criteria for aluminum and IMC layers were combined together and tested to examine their efficacy. Figure 19 shows four different fracture criteria sets tested in this study for predicting the failure modes of the six samples. For the IMC layer, two different fracture criteria were considered as shown in the figure. For the aluminum, the estimated fracture strain curves (i.e., Sets #1, 2, 3) and their variants (i.e., Set #4) were considered with addition of shear fracture curves (i.e., blue-colored fracture strain curves in Sets # 3, 4).

Initial simulations were conducted based on the four fracture criteria sets by assuming that the IMC fracture strength does not change during the baking process. This means that the same fracture strength value was adopted for the IMC layer of the six sample conditions. Note that the property data for IMC layer could not be obtained from the nano-indentation test and therefore the simulations were performed based on the assumption/adjustment of IMC fracture strength level. The simulation results show that the fracture modes of LS sample were not well captured from any of the four fracture criteria sets although the facture modes of CP and CT samples were well captured.

From these observations, it was assumed in the next simulations that the IMC fracture strength can change during the baking process. Note that, due to the difference in the coefficient of thermal expansion (CTE) of aluminum and IMC layers, the local cracking may occur along the IMC-aluminum interface during the baking process, which can be considered as lower IMC fracture (or bonding) strength in 2BK condition. With the assumption of an IMC fracture strength that is affected by the baking process, the four fracture criteria sets generally result in the matched failure modes for the six sample conditions. Figure 20 shows the predicted failure modes for the six sample conditions based on the fracture criteria Set #4. In the figure, the red-colored texts below each figure represent the failure modes observed in the seven experiments. In experiments, CT samples tend to show IF mode for 0BK and 2BK conditions, and LS samples tend to show BP mode for 0BK condition and IF mode for 2BK condition. It is noted here that the simulations based on the other three fracture criteria sets also showed the failure modes similar to those in the figure.

Table 2 shows the expected difference in IMC fracture strength between 0BK and 2BK conditions. These values were estimated such that the four fracture criteria sets can result in the matched failure modes. As the different fracture criteria were adopted in the four sets, the estimated fracture strength values are different from one another. It is however interesting that the fracture strength ratios between 0BK and 2BK conditions are very similar among the four sets such that the fracture strength for 2BK condition is about 0.5~0.6 of that for 0BK condition. It appears from these simulations that the fracture modes, especially for LS sample, can be well captured by considering different IMC fracture strength for 0BK and 2BK conditions. These simulation results suggest that possible change in bonding strength of IMC layer during baking process might be one of important factors influencing on the fracture mode. As mentioned, the local cracking may appear along the IMC-aluminum interface during the baking process from different sources (e.g., CTE mismatch between the IMC, steel, and aluminum, residual stress change within/near the nugget, etc.), which leads to lower bonding strength.

Bonding strength of IMC layer was measured to be generally <100 MPa from the tests of mini tensile bar machined from weld nugget region [1110]. Here, the measured values can literally indicate the bonding strength between the IMC layer and aluminum material. However, in the current modeling, the IMC layer is modeled using solid elements and also perfectly bonded to the neighboring elements of aluminum and steels. Then, IF failure mode is simulated by removing the failed elements from the IMC layer. For this reason, the concept of IMC fracture strength in the current modeling is not the same as the bonding strength measured from experiments. Therefore, the IMC fracture strength level (i.e., 1000~2000 MPa) estimated in this study can be much higher than the experimentally measured values. It is noted that the IMC fracture strength in the current modeling is a material parameter that can be calibrated as needed, and it can still be a qualitative indicator for the bonding strength of IMC layer.

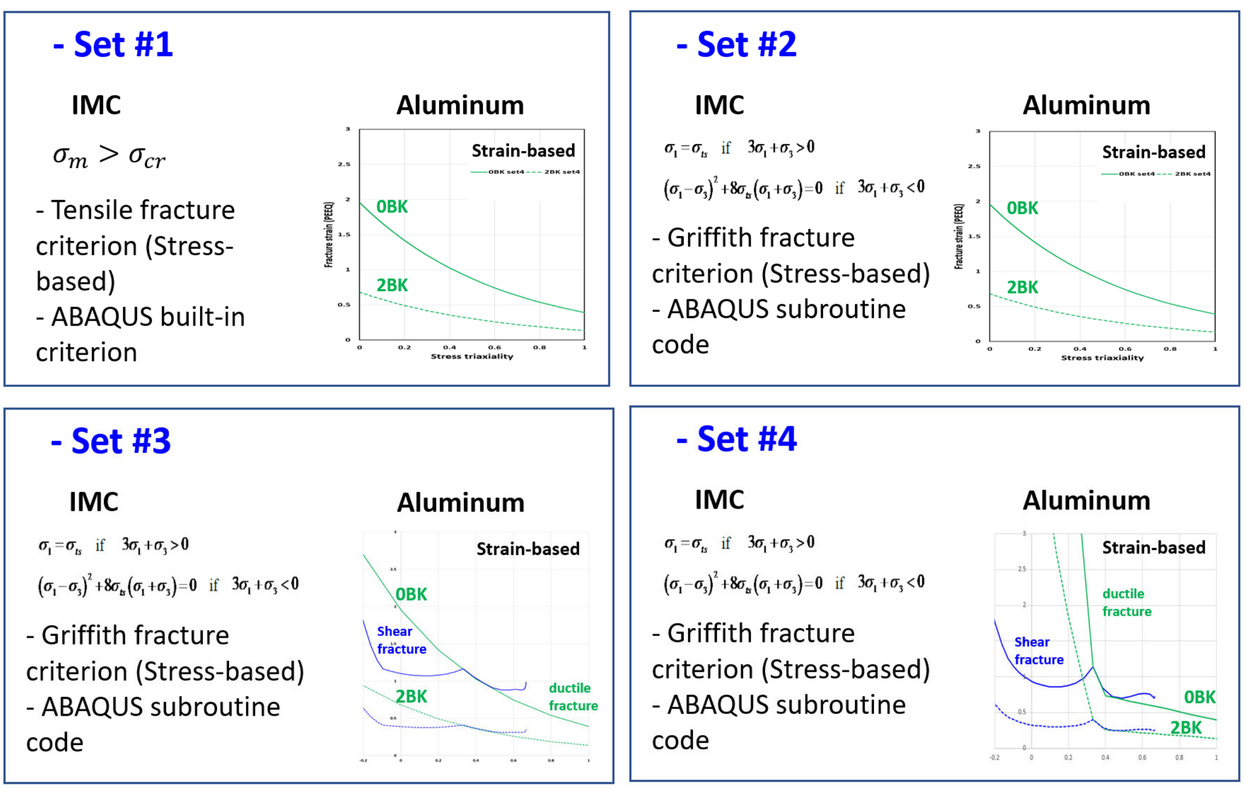

Figure 19. Four different fracture criteria sets tested for predicting failure modes of aliminum-steel weld joint of E141 material combination.

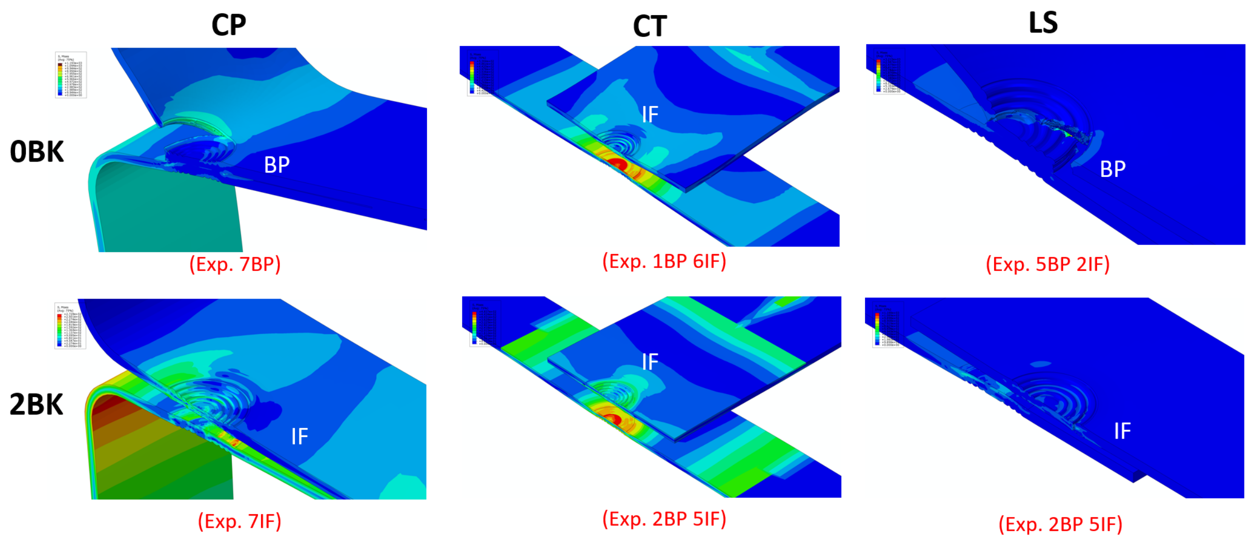

Figure 20. Examples of predicted failure modes for different samples and baking conditions based on the four fracture criteria.

Table 2. Expected difference in IMC layer fracture strength for 0BK and 2BK conditions.

	Set #1	Set #2	Set #3	Set #4
0BK	1800	2500	2100	1900
2BK	1000	1300	1200	1100
Ratio ($\sigma_{2BK}/\sigma_{0BK}$)	0.56	0.52	0.57	0.58

5.2 Modification of aluminum fracture strain curve based on dome height test

Although the model's predicted fracture modes matched with the experimental observations by introducing different IMC fracture strength for 0BK and 2BK conditions as shown in the previous section, the load-extension curves also need to be well captured in order to better understand about the key influencing factors on the failure modes. Therefore, the load-extension curves were obtained for the six sample conditions and compared with experimental curves. However, the results showed that the predicted peak loads of the load-extension curves are a lot higher (generally 50~100% higher) than the experimental values. Note that the peak loads for the samples showing IF failure mode (i.e., CP/2BK, CT/0BK, CT/2BK, LS/2BK) can be easily matched with adjusting the IMC fracture strength level which is a simple material parameter in this modeling. However, for the samples showing BP failure mode (CP/0BK, LS/0BK), matching the load-extension curve is not as simple as in the case of IF mode because the cracking/tearing of aluminum sheet, hence the aluminum fracture strain curves, are associated with the BP mode.

It was observed from the modeling that the stress triaxiality near the crack tip when the cracking occurs are approximately η=1.5~2.5 for CP/0BK sample and η=0.5~1.0 for LS/0BK sample (see Figure 26). This indicates that the aluminum fracture strain level in these triaxiality range can have dominant effects on the peak load of load-extension curves. Note that our initial fracture strain curves for aluminum were estimated only based on the tensile test (η=0.33) and then their stress triaxiality dependency was assumed to follow the curve shape shown in Figure 17(a). This suggests that the stress triaxiality dependency of the used aluminum fracture strain curves may not be very accurate for the current aluminum material.

In an effort to develop more representative stress triaxiality dependency data, Limiting Dome Height (LDH) tests were performed to obtain the aluminum fracture strain level for biaxial loading condition (η=0.66). With these additional experiments, it is expected that more accurate stress triaxiality dependency of the fracture strain curves will be obtained. Figure 21(a) and Figure 21(b) show the examples of LDH test and simulation for estimating the aluminum fracture strain level for biaxial loading condition. Note that the element size used in the model are the same as those near the crack tip of weld nugget region. Figure 21(c) and Figure 21(d) show the comparisons of load-stoke curves between simulations and experiments for 0BK and 2BK conditions. As shown in the figure, the peak load points (initiating of cracking during LDH tests) were to be matched between simulation and experiment to estimate the aluminum fracture strain level for biaxial loading condition. In the figure, the discrepancy in the load level between simulation and experiment is possibly due to the anisotropic yield behavior of the aluminum material. Note that the stress-strain curves only for the rolling direction were adopted for the aluminum in the current modeling for simplicity.

Based on these experiments and simulations, the aluminum fracture strain level for η=0.66 was determined for 0BK and 2BK conditions. Then, the aluminum fracture strain curves were modified using these new data points. Figure 22 shows the newly modified aluminum fracture strain curves compared with the original ones. As shown in the figure, stress triaxiality dependency was substantially changed for both 0BK and 2BK conditions. Interestingly, the change of fracture strain level for η=0.66 are the opposite for 0BK and 2BK conditions, showing the decrease for 0BK condition and the increase for 2BK condition. These newly modified fracture strain curves were used for the next simulations tasks.

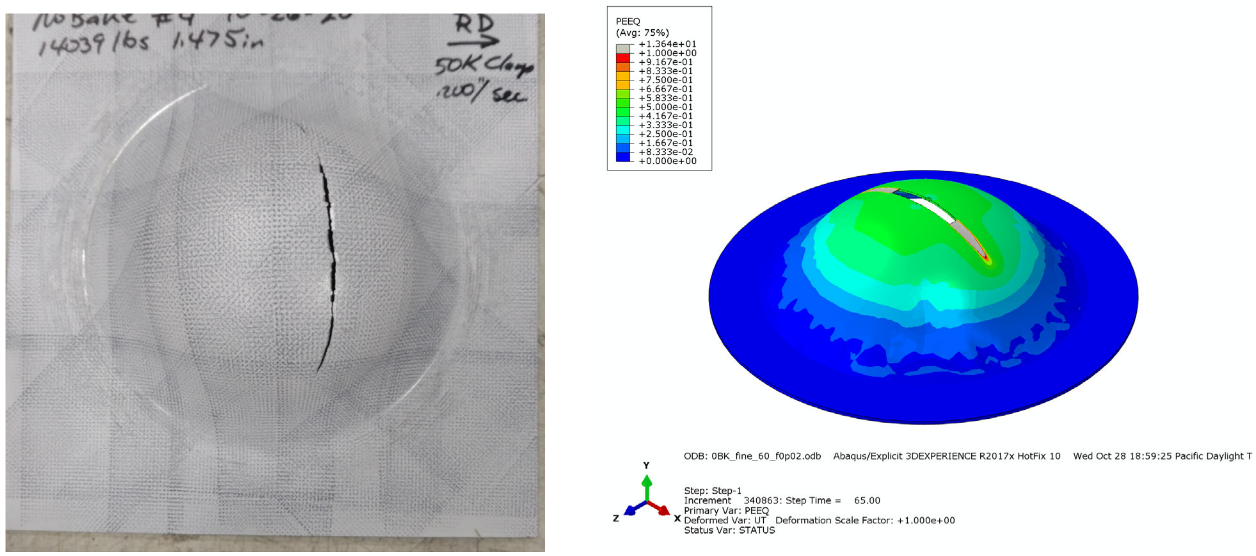

(a) (b)

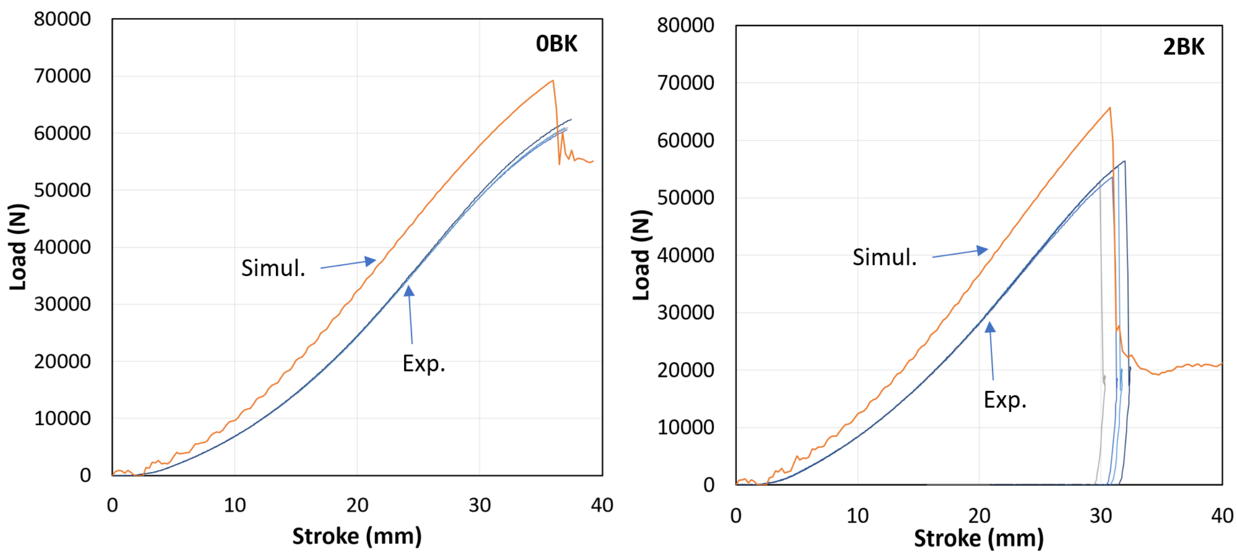

(c) (d)

Figure 21. (a) Experiment and (b) simulation for estimating the fracture strain level under biaxial loading condition. Comparison of similated load-stroke curves with experimental ones for (c) 0 baking and (d) 2 baking conditions.

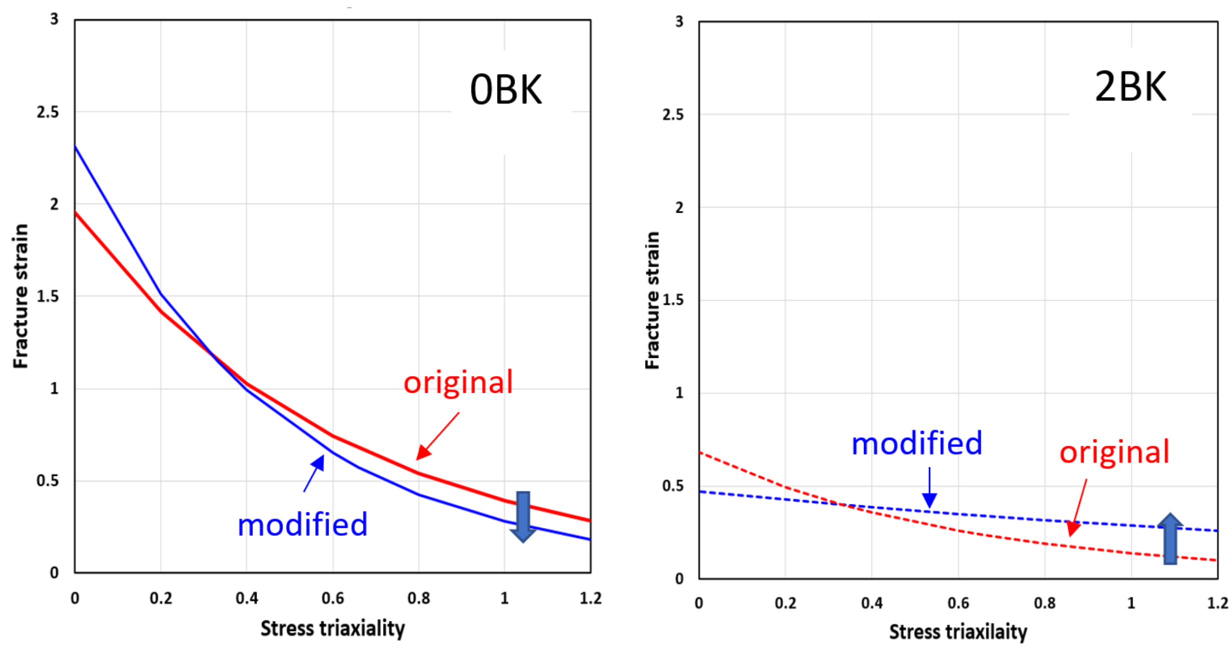

(a) (b)

Figure 22. Aluminum fracture strain curves modifed from the origianl ones based on dome height test and simulations for (a) 0BK and (b) 2BK conditions.

5.3 Simulation of coach peel sample

The modified aluminum fracture strain curves were first adopted for simulations of CP sample. Griffith fracture criterion with various IMC fracture strengths was also adopted in the simulations. For 0BK conditions, BP mode can always be obtained using the IMC fracture strength larger than 1200 MPa, indicating 1200 MPa is the lower-limit IMC fracture strength that can induce the aluminum cracking. For 2BK conditions, IF mode can be obtained with the IMC fracture strength lower than 1100 MPa, indicating the 1100 MPa is the upper-limit IMC fracture strength that can lead to interface failure at the IMC layer. As mentioned in the previous section, the peak loads for CP/2BK samples can be easily matched by adjusting the IMC fracture strength level. Therefore, the load-extension curves for CP/0BK sample showing BP mode can be of more interest in this section.

Figure 23 compares the load-extension curves based on the new aluminum fracture strain curves with the experimental ones. The simulation also indicates the BP failure mode. As shown in the figure, the peak load and overall shape of the predicted load-extension curve generally well match with the experimental curves except for the initial slope of the curve. The large discrepancy in the initial slope may be due to various sources. For example, the modeling may not have considered the accurate grip locations. Another possibility is that the welding residual stresses were not considered in the modeling. Effects of some possible sources were examined using modeling approaches. It was found that one major source for the discrepancy can be off-normal bend angle that actual CP samples have (See Figure 24(a)). FE models were modified such that they have some off-normal bend angles (i.e., 3°, 5°, 10°) (See Figure Figure 24. (a) Actual coach peel sample shape with off-normal angle, (b) an example model with off-normal bend angle and (c) effects of sample bend angle on initial slope of load-extension curves.(b)). It was observed from simulations that the off-normal bend angle can have substantial effects on the initial slope since it is directly related with the moment arm between loading point and weld nugget. The slope decreases with the increase of off-normal bend angle (See Figure 24(c)). The result shown here may suggest that the modified aluminum fracture strain curves can well capture the failure mode and load-extension curves for CP/0BK sample.

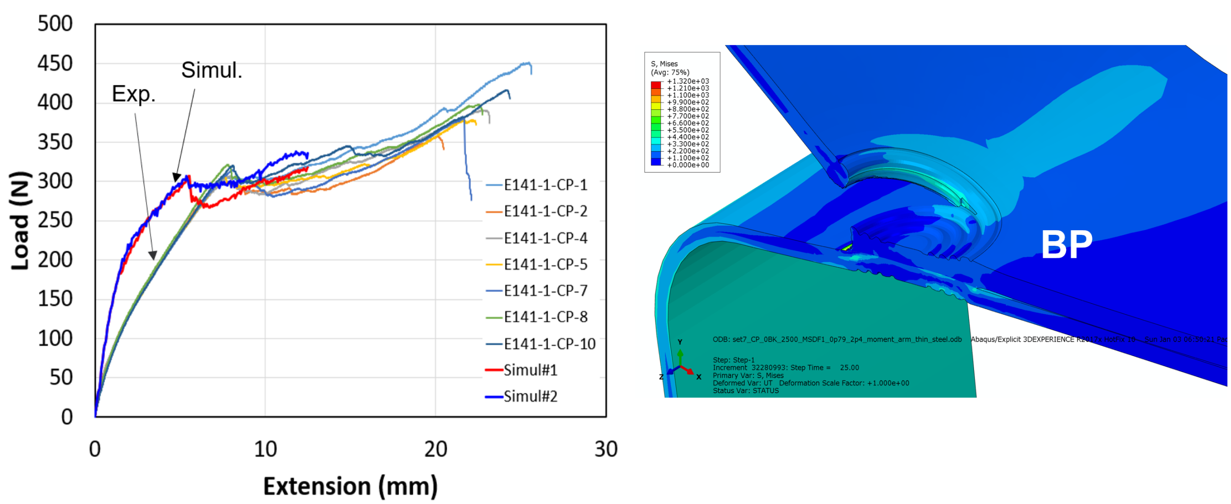

(a) (b)

Figure 23. (a) Comparison of load-extension curves between simulations and experiments for 0BK coach peel samples and (b) button pull-out failure mode from simulation.

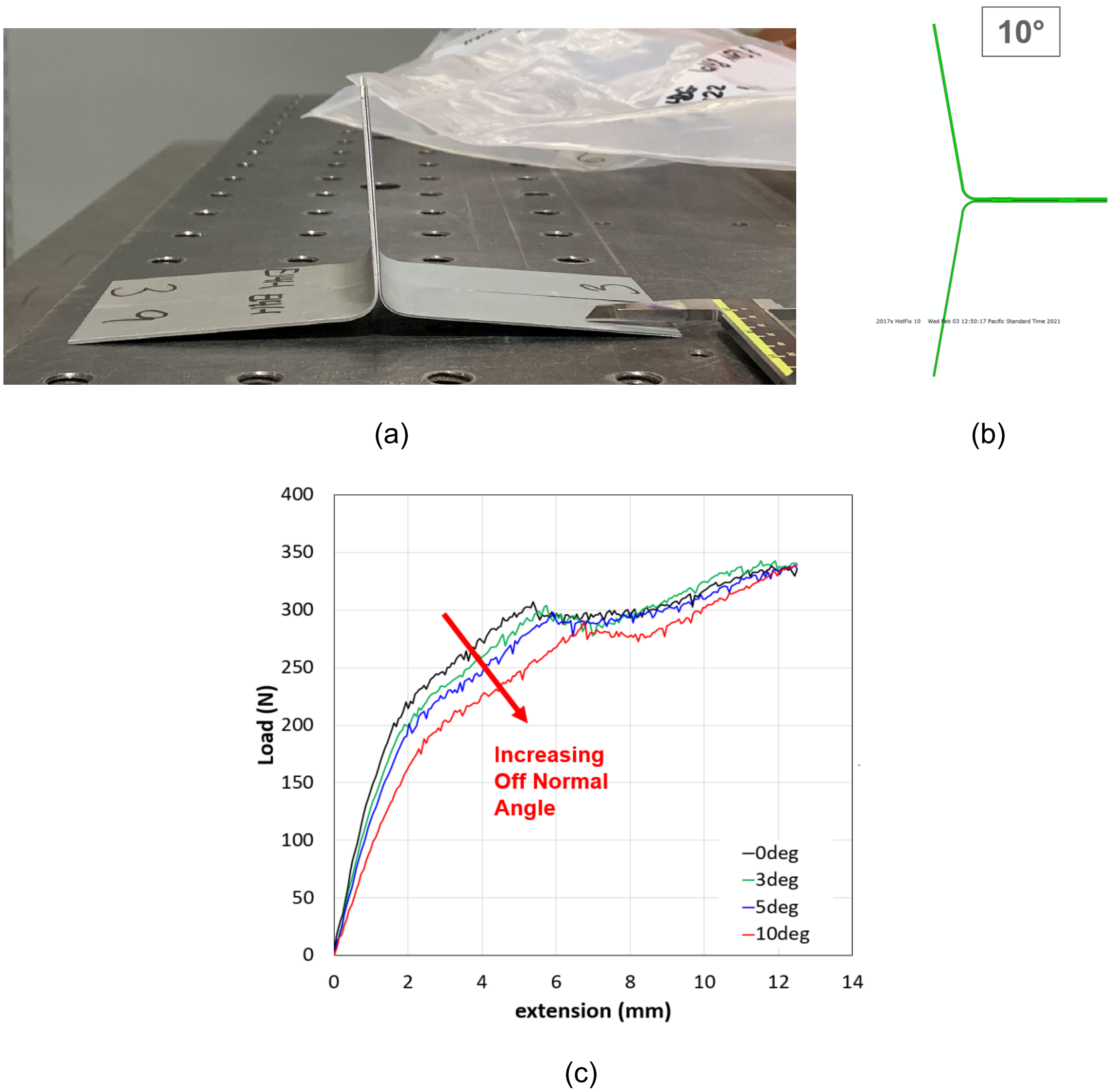

Figure 24. (a) Actual coach peel sample shape with off-normal angle, (b) an example model with off-normal bend angle and (c) effects of sample bend angle on initial slope of load-extension curves.

5.4 Simulation of lap shear sample with further modification of aluminum fracture strain curve

As the failure mode and load-extension curve for CP samples seem to be matched with the experimental ones as shown in the previous section, more simulations were then performed with LS sample models based on the same aluminum fracture strain curves presented in Figure 22. Figure 25 shows the comparison of load-extension curves of LS samples between simulation and experiment for 0BK and 2BK conditions.

For 2BK conditions, similar peak load and IF failure mode can be predicted with the IMC fracture strength of ~900 MPa as shown in Figure 25(b). Note that ~900 MPa IMC fracture strength here is lower than the upper-limit of ~1100 MPa mentioned in the previous CP/2BK modeling. For 0BK conditions, however, the load-extension curves show large discrepancy, especially in the peak loads, between simulation and experiment as shown in Figure 25(a). Also, it is seen that the peak load level depends on the adopted IMC fracture strength level (i.e., 1300~2500 MPa). This is because the initial failure begins and spreads in IF mode although the final failure modes are observed to be generally partial BP mode. Note that, even with the lower-limit IMC fracture strength of ~1200 MPa mentioned in the previous CP/0BK modeling, the predicted peak loads are still higher than the experiments. This indicates that the aluminum fracture strain curves may need to be further adjusted to attempt to decrease the peak loads of load-extension curves.

For further adjustment of aluminum fracture strain curves, the stress triaxiality near the edge of the weld nugget at the joint interface area when the cracking occurs were first examined for LS/0BK. The stress triaxiality values were found to be η=0.5~1.0 for LS/0BK sample (see Figure 26(b)). Secondly, the primary failure mode of LS/0BK sample and the associated stress triaxiality were also examined. Figure 27 shows the partial BP failure mode observed in experiments with LS/0BK samples and also the associated triaxiality level along the radial direction during failure, which is η=-0.1~0.15. This may suggest the need for a “W”-shaped fracture strain curve. There is also support for this finding from literatures (Li et al.[12], Ha et al 2[13], Bao and Wierzbicki [14]);. Note that the “W”-shaped fracture strain curves are the resultants of the combined shear and ductile fracture behaviors as shown in Figure 28(c).

The aluminum fracture strain curves were further adjusted based on the observations mentioned above. Figure 29 shows the further adjustment of aluminum fracture strain curve. In the figure, the blue-colored curve is the modified fracture strain curve presented in Figure 22(a). Note here that the two points estimated from tensile and biaxial tests and the curves between them were to be unchanged. Then, the curves for η=0.5~1.0 were adjusted to five different levels (i.e., A~E) in order to decrease the peak load for LS/0BK samples while the curves for η=1.5~2.5 generally remained the same in order not to induce the peak load change for CP/0BK samples. Also, the curves near zero stress triaxiality were adjusted to five different levels (i.e., 1~5) in order to induce the failure along the radial direction that can lead to BP failure mode.

Simulations were performed with different combinations of the curves A~E and 1~5 as well as different IMC fracture strength levels. Figure 30 shows the comparison of load-extension curves between simulations and experiments for LS/0BK samples based on the adjusted fracture strain curves. As shown in the figure, well-matched load-extension curves and failure mode were obtained from the combinations of D/E and 4/5 with IMC fracture strength of ~1600 MPa. Here, ~1600 MPa IMC fracture strength is higher than the lower-limit of ~1200 MPa mentioned in the previous CP/0BK modeling. It is noted that the obtained load-extension curves seem to have quite similar energy absorption to those of experiments, indicating that the current approach of adjusting the aluminum fracture strain curve can provide an acceptable prediction capability, at least for LS samples showing BP mode. However, the peak load levels are still not well-matched between simulation and experiment. In addition, the rapid load drop after the peak load is observed in simulation. Further work may need to be performed to obtain smooth load evolution near peak load region.

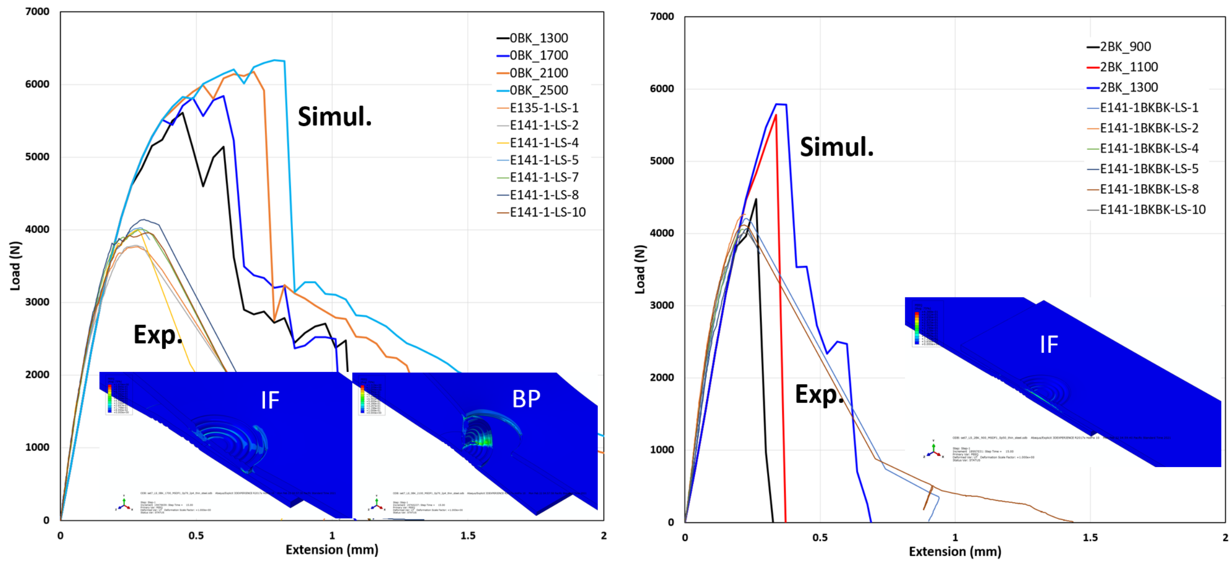

(a) (b)Frist

Figure 25. Comparison of load-extension curves between simulations and experiments for (a) 0BK and (b) 2BK lap shear samples. The simulations are based on the fracture strain curves tuned for coach peel sample model shown in Figure 22.

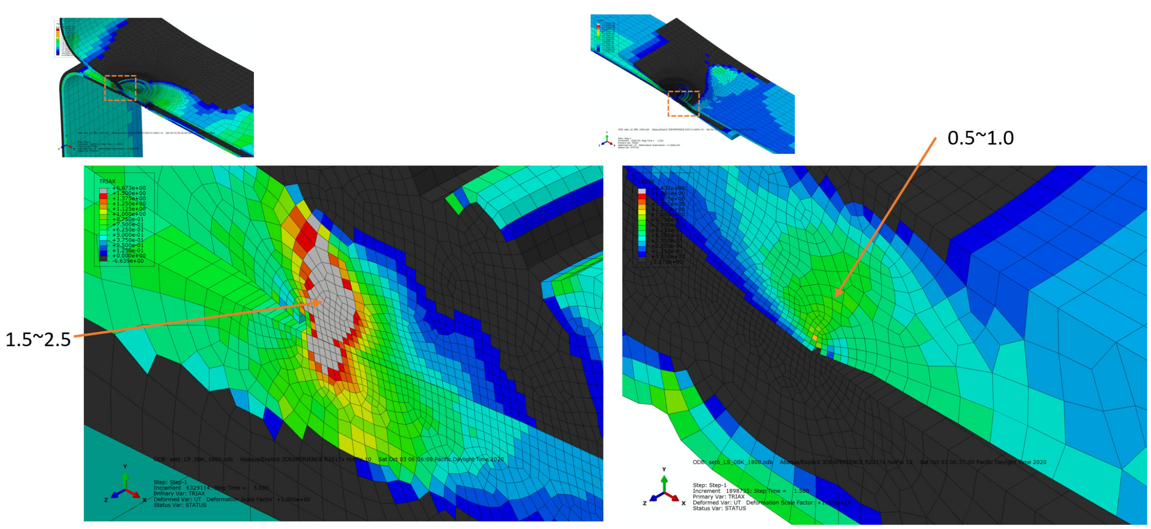

(a) (b)

Figure 26. Stress triaxiality level near crack tip of (a) coach peel and (b) lap shear samples.

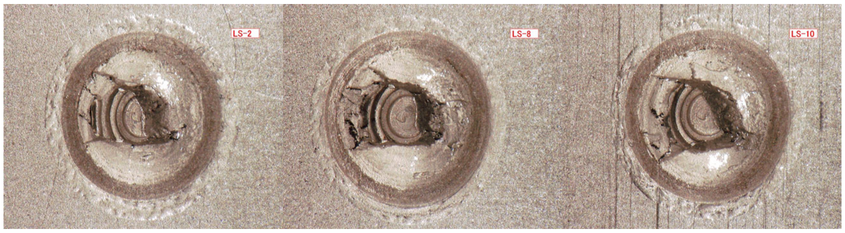

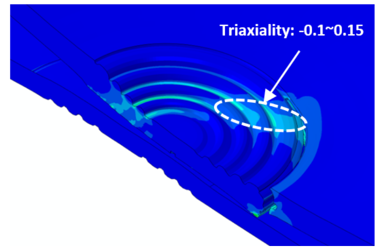

(a) (b)

Figure 27. (a) Partial button pull-out mode in lap shear samples and (b) stress triaxiality level along the radial direction during failure.

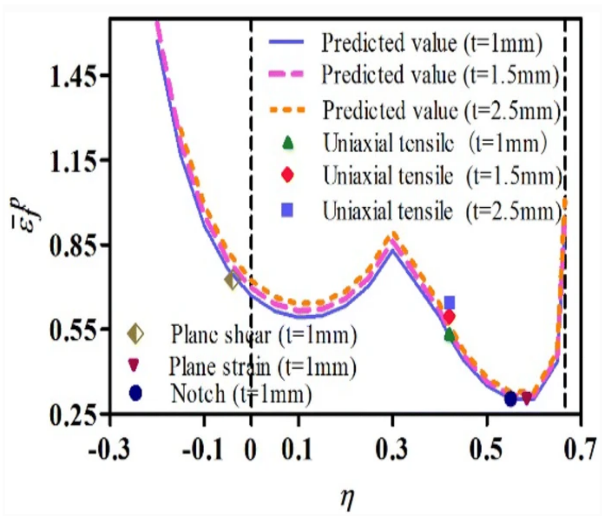

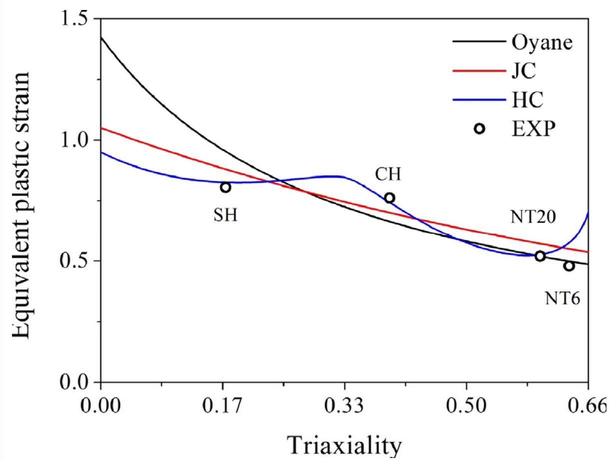

(a) (b)

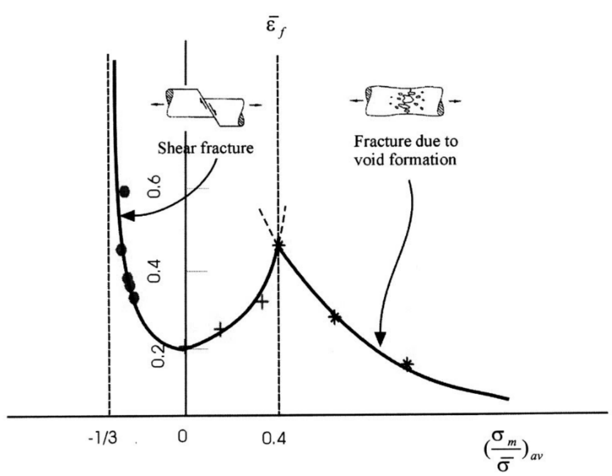

(c)

Figure 28. Fracture strain curves for aluminum as functions of stres triaxiality from literatures. (a) Li et al.[12], (b) Ha et al. [13] and (c) Bao and Wierzbicki [14]

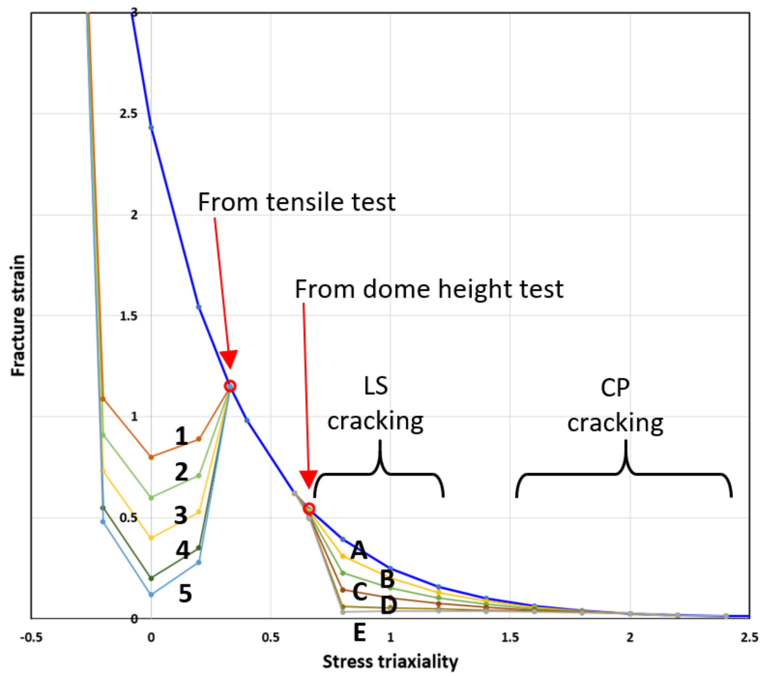

Figure 29. Fracture strain curves modified and tested for lap shear sample simulation.

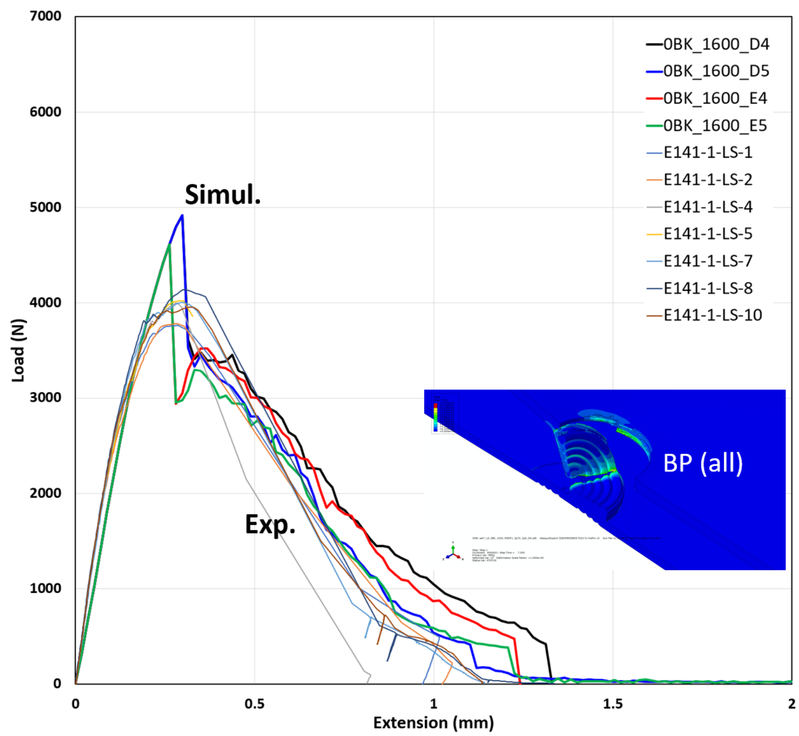

Figure 30. Comparison of load-extension curves between simulations and experiments for 0BK lap shear samples based on modifed fracture strain curves.

5.5 Consideration of kissing bond zone

It has been observed that an annulus region with some finite width and lower bonding strength can exist near the IMC layer edge at the joint interface, which is referred as the kissing bond zone. In Figure 3, darker-colored ring region is observed along the circumference of bond zone, which appears to be a kissing bond zone. The effects of lower bonding strength in the kissing zone on the peak loads of LS samples were examined in this section. For this purpose, several element layers in IMC, up to some finite width, were selected to have lower IMC fracture strength compared to the fracture strength in the central region of IMC. Figure 31(a) shows the concept of assigning lower fracture strength in the kissing bond zone. A series of simulations were performed with various combinations of widths of kissing bond zone and fracture strength levels/gradients.

Figure 31(b) shows the effects of kissing bond zone on the peak load and load-extension curves for LS/0BK samples. With the lower bonding strength in kissing zone, the peak load can decrease and also smoother load evolution can occur near peak load region as shown in the figure. However, some change in energy absorption is also observed with lower bonding strength in kissing zone. In summary, it can be said that the introduction of kissing zone is helpful to obtain reasonable peak load and its evolution with no substantial effects on the energy absorption, although the failure mode is observed to sensitive to the property parameters adopted for kissing zone.

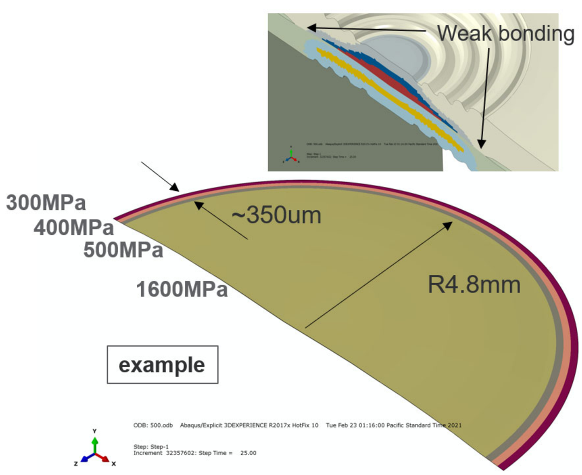

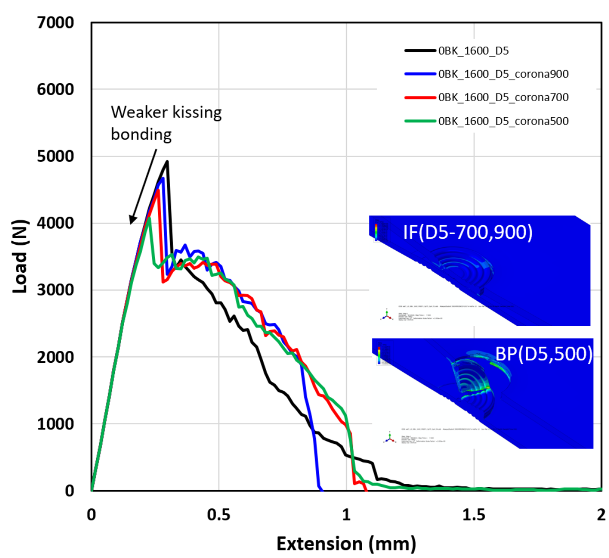

(a) (b)

Figure 31. (a) Assignment of lower fracture strength along the circumference of IMC layer and (b) effects of lower fracture strength on peak load and load-extension curves.

5.6 Simulation of coach peel sample with modified material parameters

In this section, the calibrated material parameters from LS/0BK modeling and kissing zone concept were adopted for CP/0BK samples. Theoretically, it is expected that the simulation results here should predict the load-extension curves and failure mode matched with the experiment. Figure 32 shows the simulated failure mode and the load-extension curves based on the material parameters calibrated from LS/0BK modeling. Since a high IMC fracture strength (i.e., 1600 MPa) was adopted here, BP failure mode is naturally predicted as shown in the figure. However, the predicted load-extension curves show the discrepancy compared to the experimental curves. In Figure 32(b), the black-colored curve was based on the blue-colored fracture strain curve, shown in Figure 29, which is an original curve before the adjustment for LS sample, whereas the other colored curves were based on several variants of the material parameter set calibrated from LS/0BK. It is observed that adjusting the aluminum fracture strain curve into the shape of "W" and introducing the kissing zone concept into the model resulted in some noticeable decrease in peak load as well as the rapid load drop after the peak load as shown in Figure 32(b). As mentioned, several variants were further tested for the purpose of finer property tuning in order to match the predicted peak load and post-peak behavior with the black-colored curve. However, the matched results were not obtained yet. Further works needs to be done to better understand the difficulties seen here and to solve them with a reasonable way.

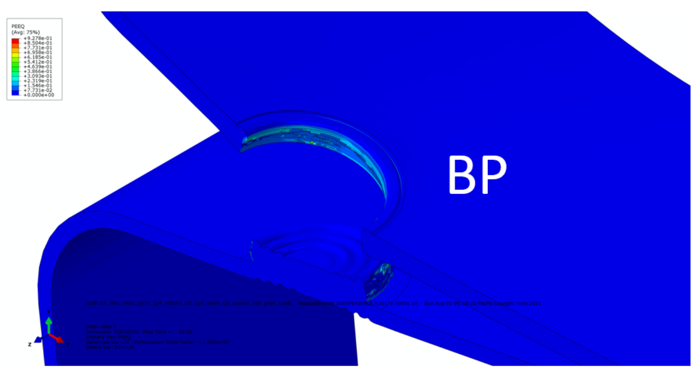

(a)

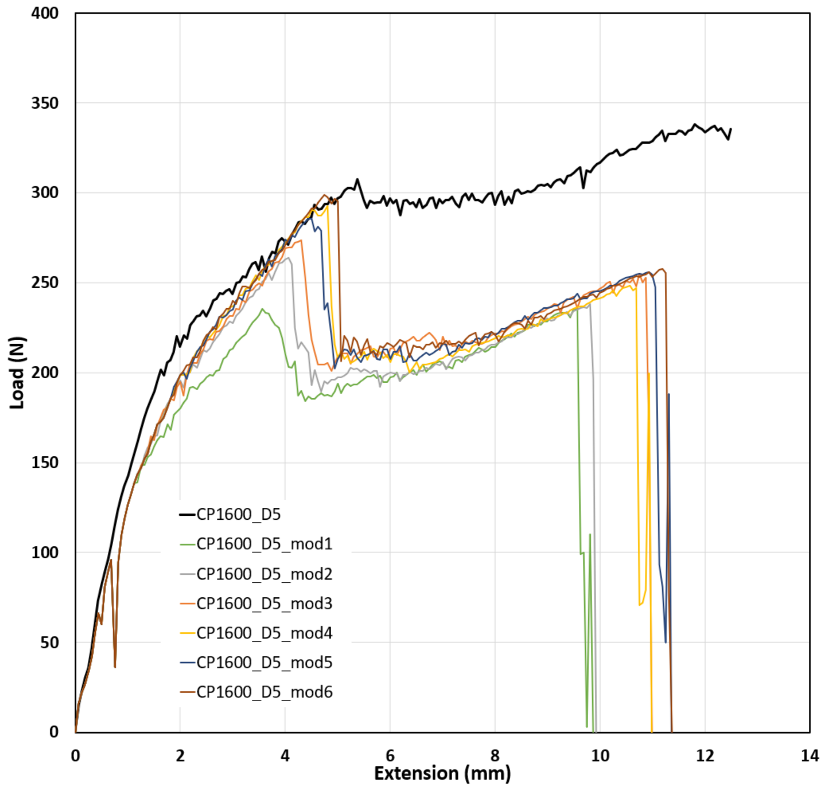

(b)

Figure 32. (a) Failure mode of coach peel sample and (b) load-extension curves based on the materials properties calibrated from LS sample modeling.

5.7 Attempts to consider weld residual stress effects

Residual stresses may occur within/near the weld nugget after welding mainly due to different CTE of the materials in these regions. Therefore, the effects of residual stress may be crucial on the failure behaviors of weld nugget. In order to consider the residual stress effects, residual stress distribution data from an earlier RSW process simulation was extracted and provided for the current FE models. The stress data was interpolated and then assigned to the elements as the initial stresses within/near the weld nugget. A static simulation was first performed to reach the equilibrium state before tensile loading is applied. Figure 33 shows the residual stress data extraction, its assignment to the model as the initial conditions and the reached equilibrium state. As show in the figure, some high level of Mises stresses (e.g., 276 MPa in IMC and 164 MPa in steel sheet) was resulted from the residual stress input before the tensile loading is applied.

The purpose of this task was to consider the effects of initial damage (i.e., initial equivalent plastic strain) due to the weld residual stresses on the damage evolution and final fracture. Since the model includes some initial damage, the failure is expected to occur earlier than the cases without consideration of residual stresses. However, this earlier failure could not be observed from the simulations. Detailed examination of the simulations results shows that the assigned initial damage is not included into the calculation of total damage accumulation. It appears that, for the non-proportional stress state where the stress state varies during the loading process, the damage accumulated in the previous step is not included in the damage calculation during next step. A user-subroutine code needs to be made in order to overcome this difficulty. However, coding a user-subroutine for this purpose was out of scope of the current project and residual stress effects could not be correctly evaluated.

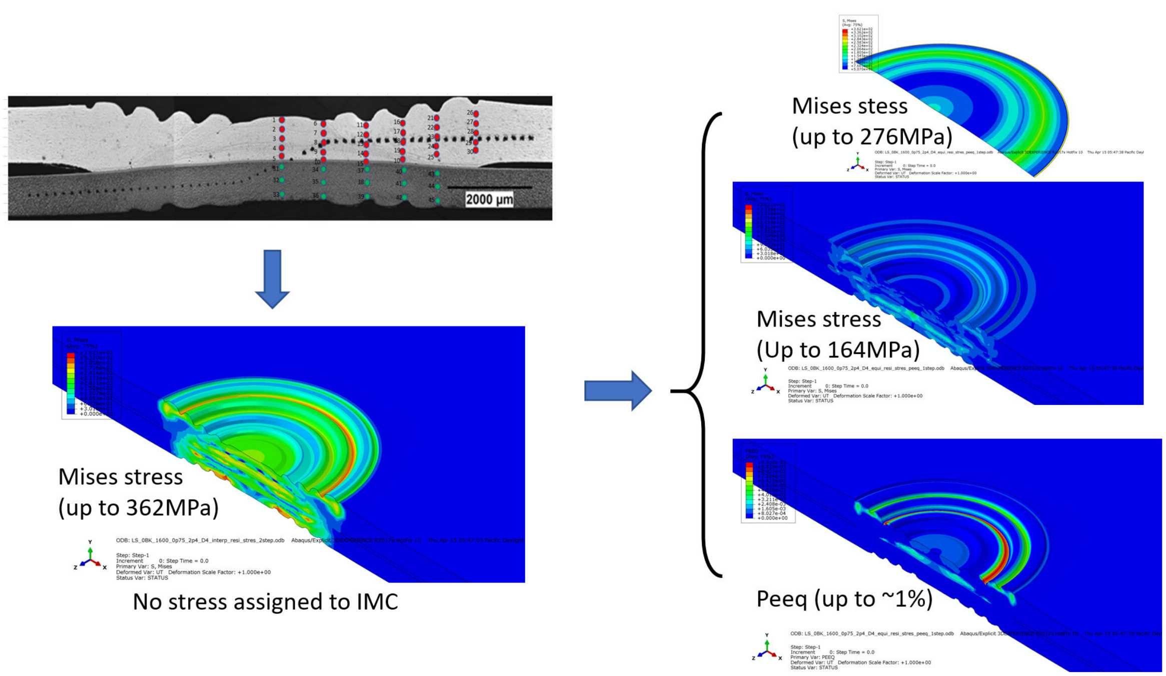

Figure 33.Tested modeling method to consider the effects of welding residual stress and its evoultions on the failure mode of weld nugget.

6.0 Conclusions

In this study, development of FE modeling methods has been conducted for the purpose of predicting the failure modes of aluminum to steel resistance spot welds. For this purpose, the weld coupons were first created with five different material combinations, and tested under three different destructive testing configurations (i.e., coach peel, cross tension and lap shear tests). Microstructural characterization and micro/nano indentation tests were also performed to evaluate the local material properties within the weld nugget region. The FE models of weld performance were then generated for a selected material combination (i.e., E141) and simulated to examine the influence of various aspects on the failure mode and load-extension curves. The model validation work has also been performed with the selected material combination by fine-tuning material parameters, which has achieved partial success in the project goal. Some key results/observations obtained from the work done so far are summarized below.

- The weld coupons of three testing configurations (i.e., CP, CT, LS) were generated with five different material combinations and three different baking conditions (i.e., 0BK, 1BK, 2BK). From tensile destructive tests, the fracture modes (i.e., BP, HB, PB, IF) are observed to be different for different material combinations and to be often changed with baking process. In addition, the failure mode is not consistent in some situations.

- Nano-indentation tests were performed with different indenters (e.g., Berkovich tip, spherical tip, flat tip). The obtained data was used for extracting local stress-stain relations within the weld nugget regions based on various methods suggested in the literatures. FE method was also explored for back-estimating the material's stress-strain curves from load-depth curves. However, no single method resulted in a universal solution with accuracy level acceptable for the objective of this task.

- Microhardness tests were performed across the weld nuggets for all weld/baking conditions. Tensile properties were also obtained for the aluminum and steels for different baking conditions. Local properties within weld nuggets could then be estimated based on the obtained hardness-strength relationship.

- Weld simulation FE models were generated based on the actual weld geometry and the observations of microstructures. Stress-strain curves estimated from micro hardness values were assigned for different zones of aluminum and steel within weld nugget. Strain-based ductile damage was adopted for aluminum, which depends on stress triaxiality. IMC layer was modeled using solid elements and the stress-based brittle fracture criteria. In this modeling, the failure mode (i.e., BP or IF) can be determined by the competition between aluminum fracture strain level and IMC fracture strength level.

- First simulation tasks were performed for predicting the matched failure modes of the selected material combination for different conditions (i.e., CP/CT/LS, 0BK/2BK) by testing different fracture criteria and adjusting their critical values. It is found that the matched failure modes for all conditions can be predicted only by assuming lower IMC fracture strength with baking process. This indicates that possible weakening in bonding strength of IMC layer, due to local cracking, during baking process may be one of important factors influencing on the fracture mode.

- Limiting dome height tests were performed to obtain more accurate stress-triaxiality dependency of aluminum fracture strain curves for predicting better matched load-extension curves. The aluminum fracture strain curve modified based on the LDH tests, along with a strong-enough IMC fracture strength, was helpful to enable accurate prediction of the load-extension curve and BP failure mode of CP/0BK samples. Weaker IMC fracture strength appears to be a key factor influencing on the load-extension curve and IF failure mode of CP/2BK samples. Off-normal bend angles of actual CP samples can have significant effects on the initial portion of load-extension curves.

- Further adjustment was performed on the aluminum fracture strain curves, modified based on LDH tests, for predicting better matched load-extension curves and failure mode of LS samples. W-shaped aluminum fracture strain curves as function of stress triaxiality appear to enable accurate prediction of the overall shape of load-extension curve and HB failure mode of LS/0BK samples. Consideration of weaker bonding in kissing zone can help to better predict the peak load of LS/0BK samples. Similar to the case of CP/2BK, weak IMC fracture strength can also be a key factor influencing on the load-extension curve and IF failure mode of LS/2BK samples.

- The calibrated material parameters from LS/0BK modeling and kissing zone concept are theoretically expected to predict the matched load-extension curves and failure mode for CP/0BK samples. However, the newly predicted load-extension curves for CP/0BK samples show noticeable discrepancy compared to the experimental curves. Further fine-tuning works need to be done to solve these issues.

- Model validation and refinement efforts demonstrated that alignment between model and experimental results is possible in a number of cases, but is yet to be universal. This can be attributed to the complexity of predicting both the failure modes and load-extension curves for different sample configurations and baking conditions. The authors have identified a number of opportunities for improvement of the model that should enable a better understanding of the failure mechanisms of spot welding of dissimilar materials.

7.0 Recommendations

In this project, model validations activities were to be completed against the selected material combination for different testing configurations and baking conditions. Then, the developed modeling method was to be applied to the other material combinations in order to understand additional fundamentals and the key factors influencing on the failure mode of aluminum to steel spot welding. While the model accuracy is not 100% satisfactory, significant strides towards the development of a model to predict failure mode as well as load displacement curves has been made here. Based on the results and observations obtained so far, further refinement activities may be recommended to help to achieve the project goals.

- Finer tuning of aluminum fracture strain curves and kissing bond strength : Tuning of aluminum material parameter including fracture stains and kissing bond strength etc. tuning is yet to be performed such that they can satisfy the failure modes for both of CP and LS samples.

- Examination of aluminum properties near edge of the weld nugget and interface of the aluminum/steel : Here, the assignment of local properties within aluminum nugget region in the FE model was based on the microhardness values across the nugget center regions. It can be recommended that the local properties near edge of the weld nugget are experimentally examined to check if they show similar features to the assigned properties.

- Perform model/ experimental result comparisons for additional joint configurations : Modeling/simulations for other joining conditions and configurations (i.e., CT sample, 1BK conditions) are to be performed to do a complete validation of the modeling method.

- Completion of the implementation of the residual stress FE into the model : Welding residual stress effects are to be considered to have better understanding the failure behavior of the joints. A new user-subroutine needs to be coded to correctly implement these effects in FE models.

- Consideration of material anisotropic behavior : In the current modeling, the anisotropic deformation behaviors of aluminum materials were not considered. For future modeling, these behaviors may need to be considered to more accurately capture the failure behaviors of aluminum weld nugget.

- Application of the modeling method to other material combinations : Other material combinations are to be modeled and analyzed to understand the key factors influencing on the failure modes.

8.0 References

1 Carlson, B. E. (2017) “Developing resistance spot welding processes for joining 6XXX aluminum alloys to zinc coated steels”, 70th International Institute of Welding Annual Assembly and International Conference, Shanghai, China, June 27, 2017.

2 Sigler, D. R., Schroth, J. G. and Karagoulis, M. J. (2012) “Weld electrode for attractive weld appearance”, U.S. Patent 8,222,560, July 17, 2012.

3 Chen, J., Feng, Z., Wang, H.-P., Carlson, B. E., Brown, T. and Sigler, D. (2018) “Multi-scale mechanical modeling of Al-steel resistance spot welds”, Materials Science and Engineering A 735: 145-153.

4 Cheng, G., Choi, K. S., Hu, X. and Sun, X. (2016) “Determining individual phase properties in a multi-phase Q&P steel using multi-scale indentation tests”, Materials Science and Engineering A 652: 384-395.

5 Dao, M., Chollacoop, N., Van Vliet, K. J., Venkatesh, T. A. and Suresh, S. (2001) “Computational modeling of the forward and reverse problems in instrumented sharp indentation”, Acta Materialia 49: 3899-3918.

6 Tabor, D. (1951) “The hardness of metals”, Clarendon Press, Oxford.

7 Cao, Y.P. and Lu, J. (2004) “A new method to extract the plastic properties of metal materials from an instrumented spherical indentation loading curve”, Acta Materialia 52: 4023-4032.

8 Hu, X. H., Choi, K. S., Sun, X. and Golovashchenko, S. F. (2014) “Edge fracture prediction of traditional and advanced trimming processes for AA6111-T4 sheets”, Journal of Manufacturing Science and Engineering 136: 021016-1-11.

9 ABAQUS, (2017) “Abaqus 2017 User’s Manual”.

10 Jaeger, J. C. (1970) “Elasticity, fracture and flow: with engineering and geological applications”, Springer Netherlands. ISBN 978-94-011-6024-7.

11 Brown, T. W. and Sigler, D. R. (2016) “Faying interface mechanical properties of aluminum-to-steel welds as determined by microtensile testing”, General Motors Research Report CMS-289/MSR-437.

12 Li, Z., Lu, S., Yang, W. and Zhang, T. (2019) “Study on the ductile fracture rule of 6061-T6 aluminum alloy sheet under different strain conditions”, Transactions of the Indian Institute of Metals 72: 2721-2728.

13 Ha, J., Baral, M. and Korkolis, Y. P. (2018) “Plastic anisotropy and ductile fracture of bake-hardened AA6013 aluminum sheet”, International Journal of Solids and Structure 155: 123-139.

14 Bao, Y. and Wierzbicki, T. (2004) “A comparative study on various ductile crack formation criteria”, Journal of Engineering Materials and Technology 126: 314-324.

Appendix A – Load-extension curves

The load-extension curves were obtained from destructive tensile testing with weld coupons for different coupon geometries, material combinations and baking conditions, and the results are plotted below in Figure 34. The observed failure modes of the seven coupons are also included in each plot.

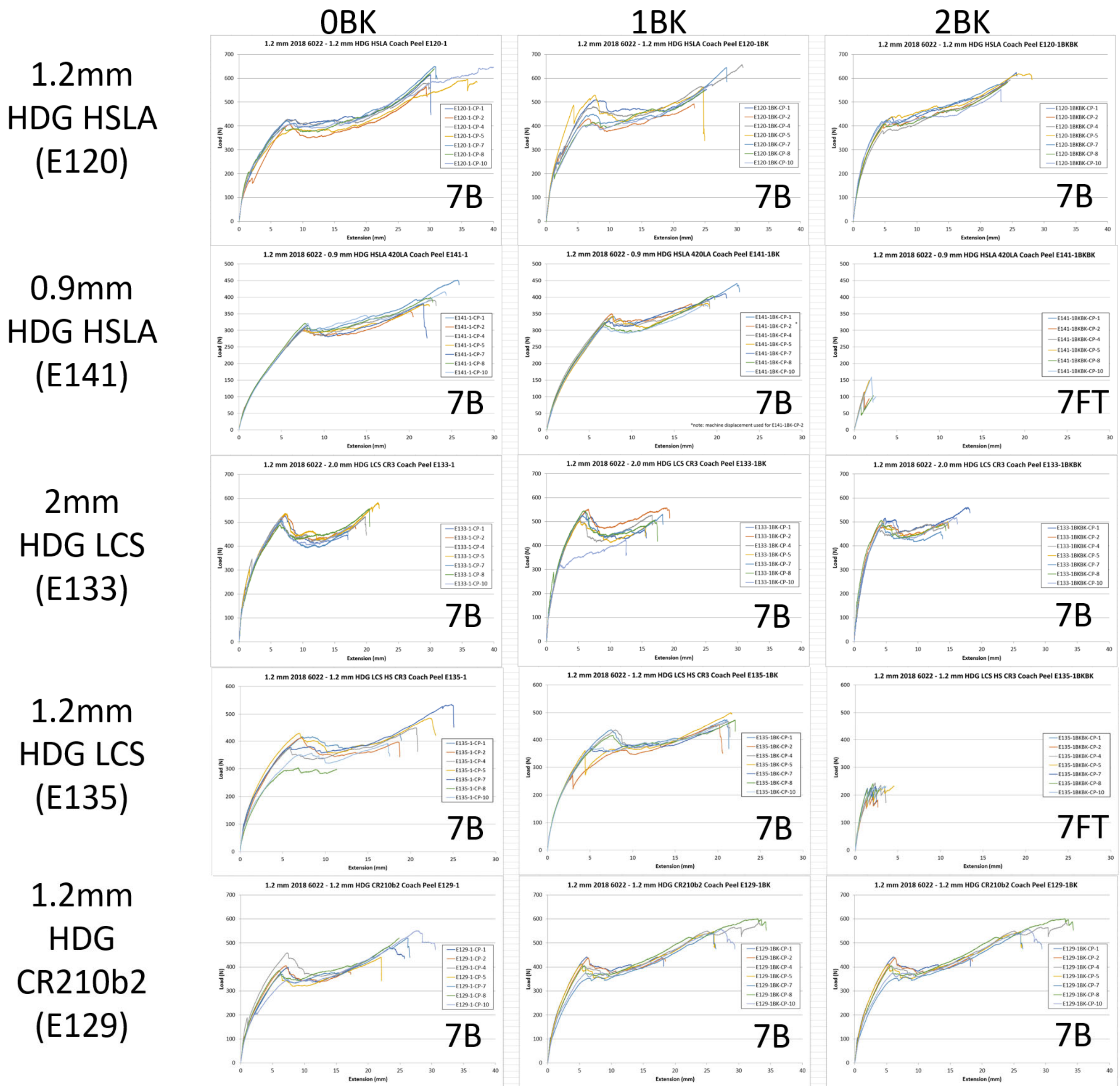

(a)

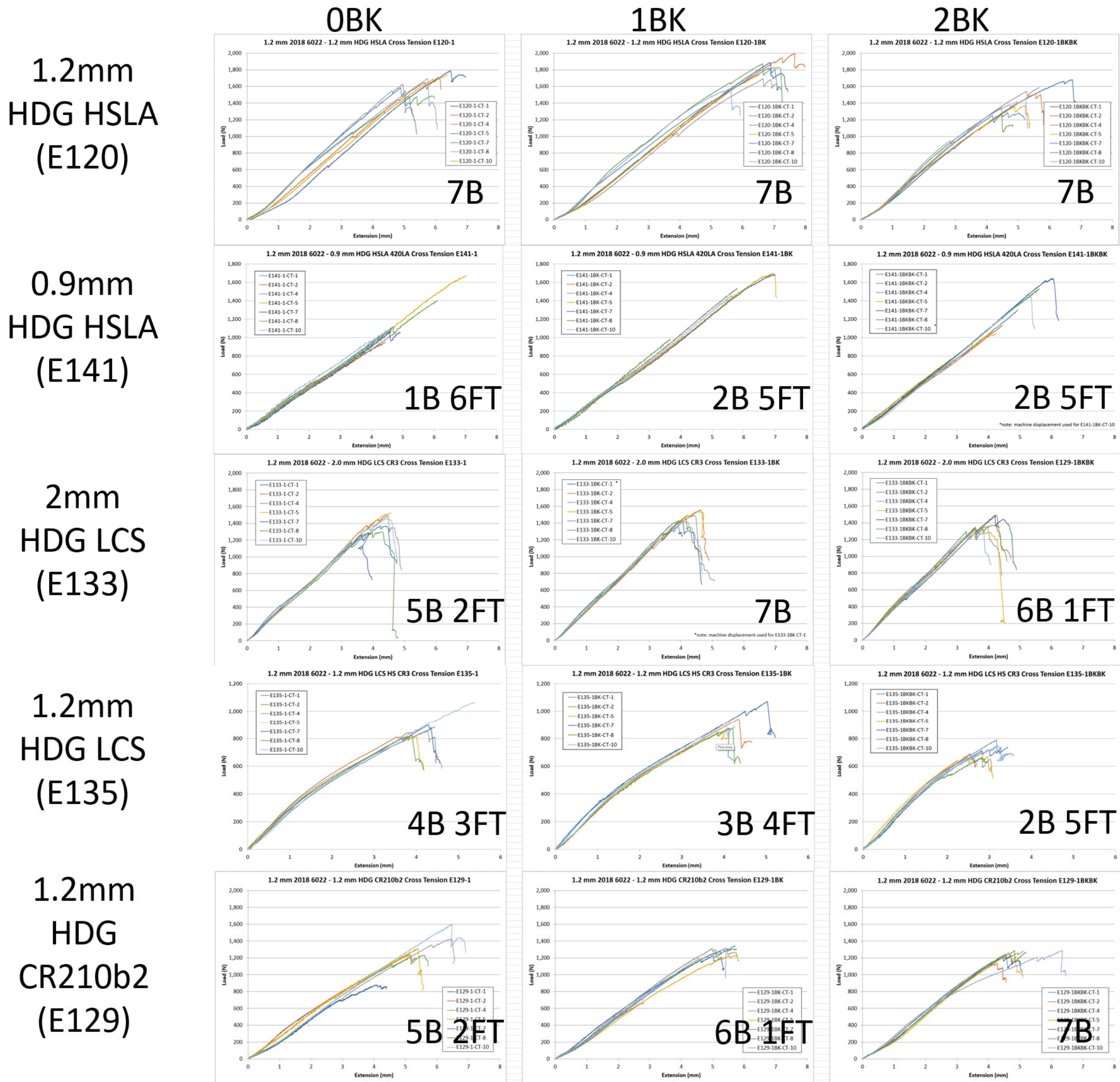
0BK
1BK
2BK
1.2mm HDG HSLA (E120)
0.9mm HDG HSLA (E141)
2mm HDG LCS (E133)
1.2mm HDG LCS (E135)
1.2mm HDG CR210b2 (E129)
1.2 mm 2018 6022 - 1.2 mm HDG HSLA Cross Tension E120-1
1.2 mm 2018 6022 - 1.2 mm HDG HSLA Cross Tension E120-1BK
1.2 mm 2018 6022 - 1.2 mm HDG HSLA Cross Tension E120-1BKBK
7B
7B
7B
1.2 mm 2018 6022 - 0.9 mm HDG HSLA 420LA Cross Tension E141-1
1.2 mm 2018 6022 - 0.9 mm HDG HSLA 420LA Cross Tension E141-1BK
1.2 mm 2018 6022 - 0.9 mm HDG HSLA 420LA Cross Tension E141-1BKBK
1B 6FT
2B 5FT
2B 5FT
1.2 mm 2018 6022 - 2.0 mm HDG LCS CR3 Cross Tension E133-1
1.2 mm 2018 6022 - 2.0 mm HDG LCS CR3 Cross Tension E133-1BK
1.2 mm 2018 6022 - 2.0 mm HDG LCS CR3 Cross Tension E129-1BKBK
5B 2FT
7B
6B 1FT
1.2 mm 2018 6022 - 1.2 mm HDG LCS HS CR3 Cross Tension E135-1
1.2 mm 2018 6022 - 1.2 mm HDG LCS HS CR3 Cross Tension E135-1BK
1.2 mm 2018 6022 - 1.2 mm HDG LCS HS CR3 Cross Tension E135-1BKBK
4B 3FT
3B 4FT
2B 5FT
1.2 mm 2018 6022 - 1.2 mm HDG CR210b2 Cross Tension E129-1
1.2 mm 2018 6022 - 1.2 mm HDG CR210b2 Cross Tension E129-1BK
1.2 mm 2018 6022 - 1.2 mm HDG CR210b2 Cross Tension E129-1BKBK
5B 2FT
6B 1FT
7B
Load (N)
Extension (mm)

(b)

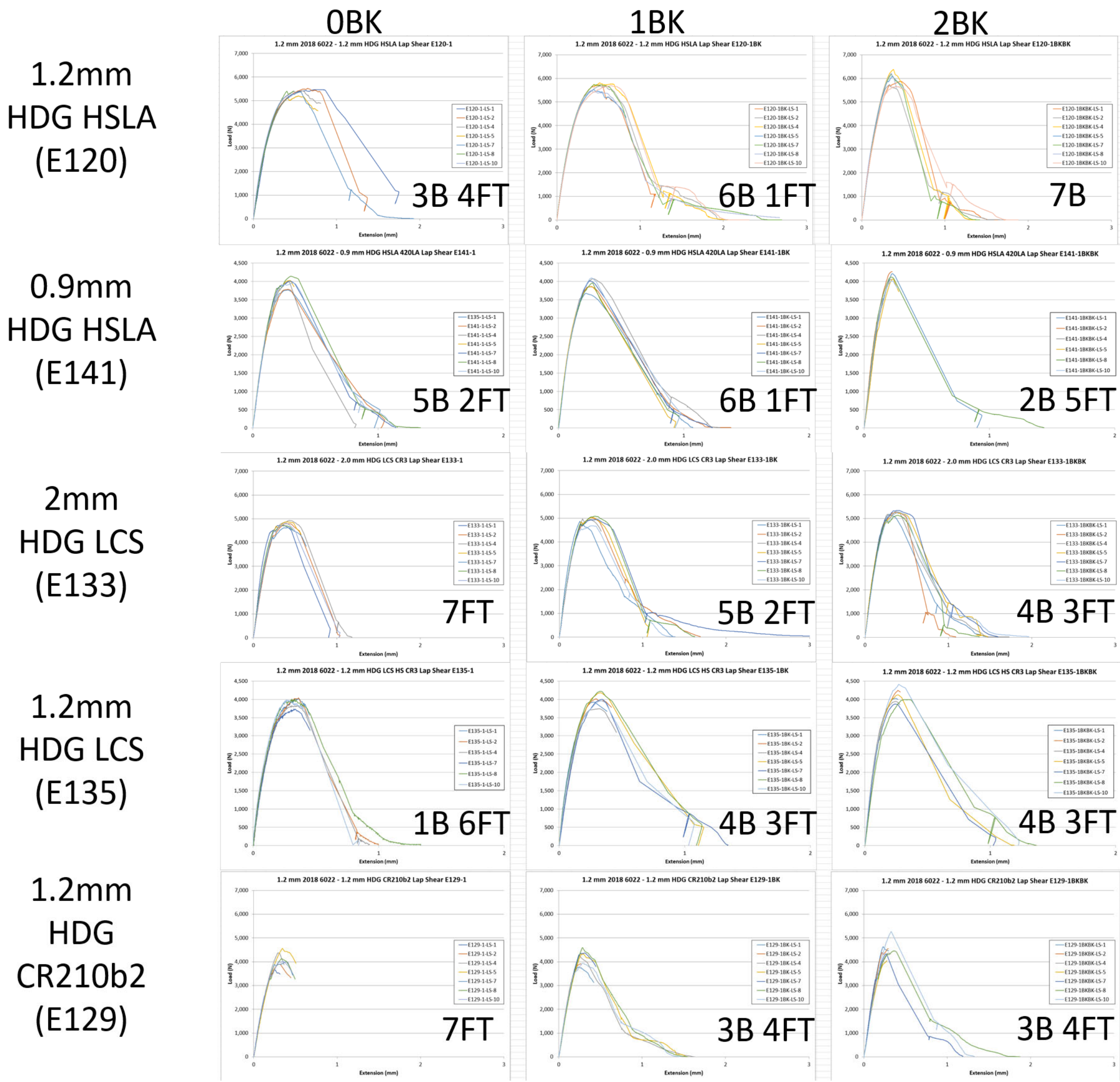

(c)

Figure 34. Load-extension curves for different welding/baking conditions and material combinations. (a) Coach peel, (b) cross tension and (c) lap shear

Appendix B – Microhardness measurement

Microhardness measurements were performed for all the welding conditions, spanning across the aluminum and steel base material, heat affected zone (HAZ) and nugget. The local property change for different material combinations and baking conditions can be evaluated from these measurements. The images of cross-sections after hardness test and the hardness data across the nugget are presented below in Figure 35. The two red arrows in the left and right point to the data at the boundaries between the base materials and the HAZ in steel, and the nugget in aluminum, respectively. The red arrow in the center points to the first aluminum hardness data near the nugget center.

1.2mm HDG HSLA (E120)

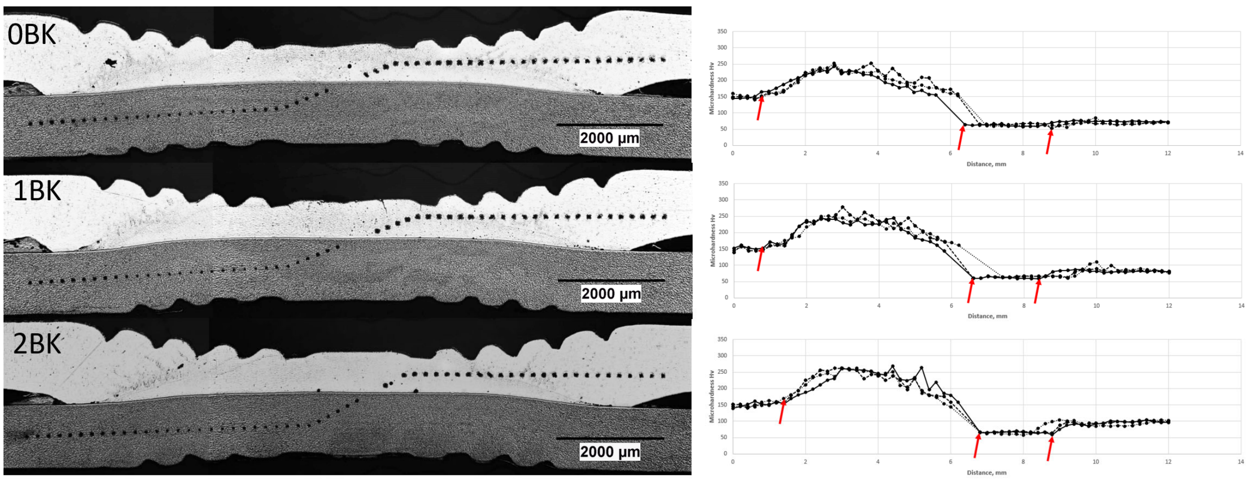

0.9mm HDG HSLA (E141)

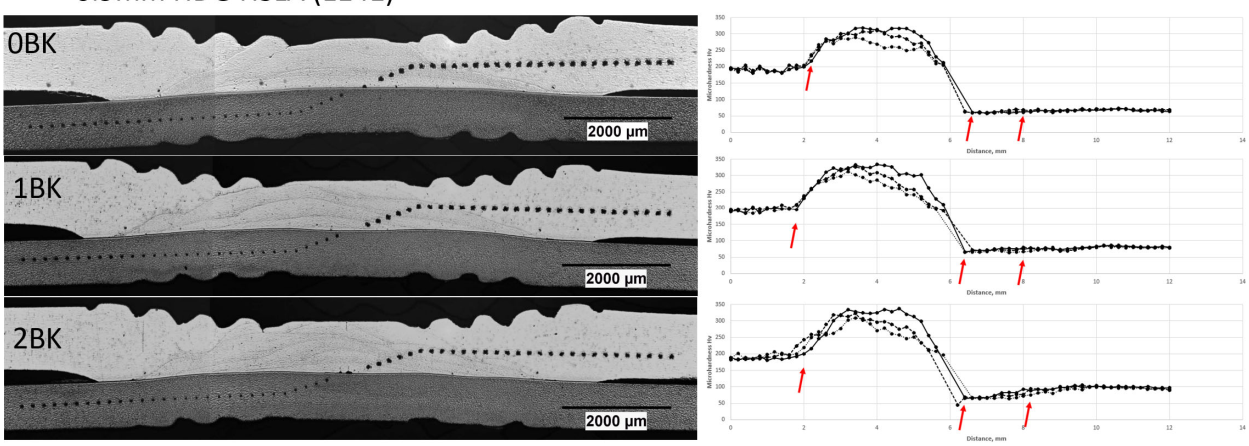

2mm HDG LCS (E133)

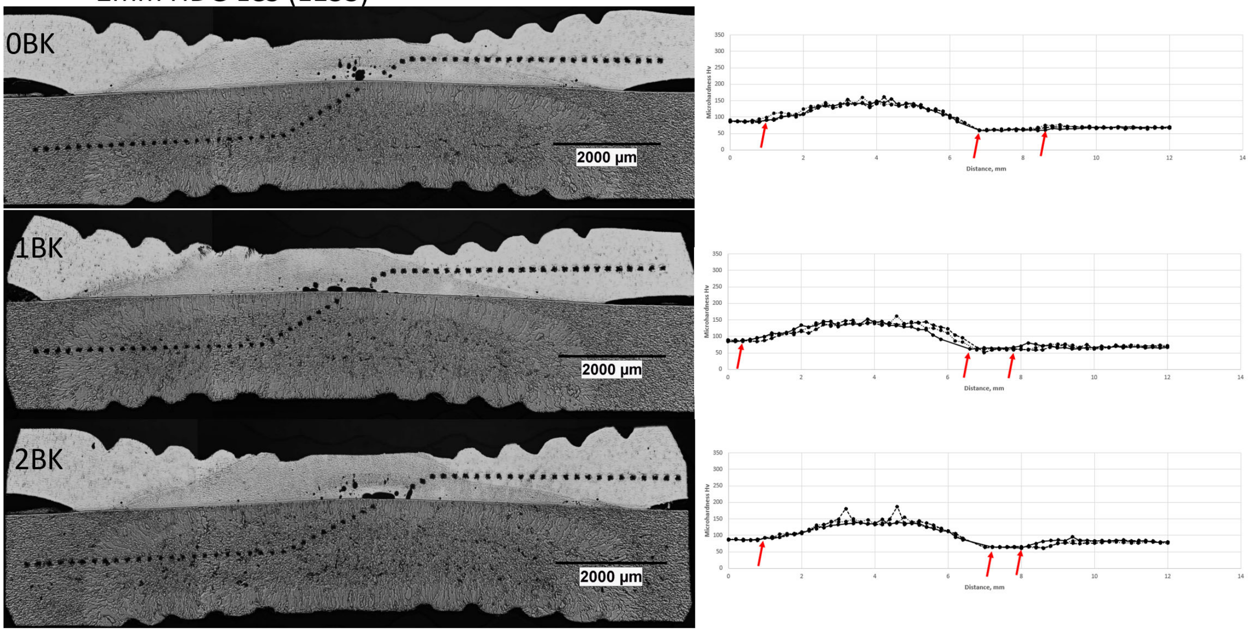

1.2mm HDG LCS (E135)

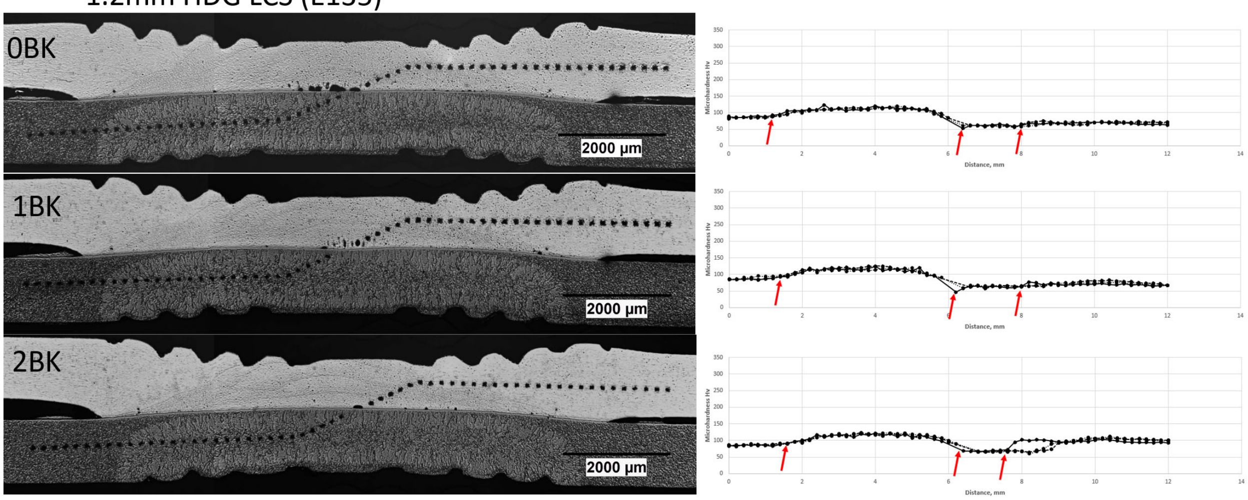

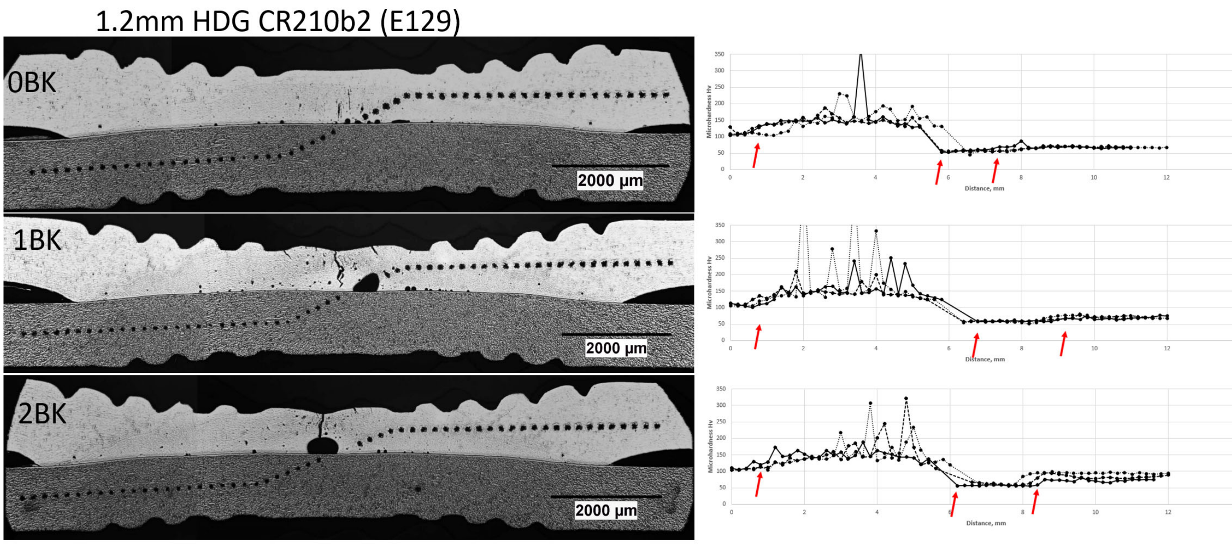

Figure 35. Microhardness measurements across the weld nugget regions for different welding/baking conditions and material combinations.

Appendix C – IMC layer thickness measurement

IMC layer thicknesses were measured along the interface line of the weld for all the material combinations and baking conditions. The measured IMC layer thickness are presented below in Figure 36. In the figure, the numbers on the right side represent the average thickness of IMC layers for each material combination. IMC layer thickness appears not to change with the baking process, but generally depends on the thickness of steel sheet of the weld.

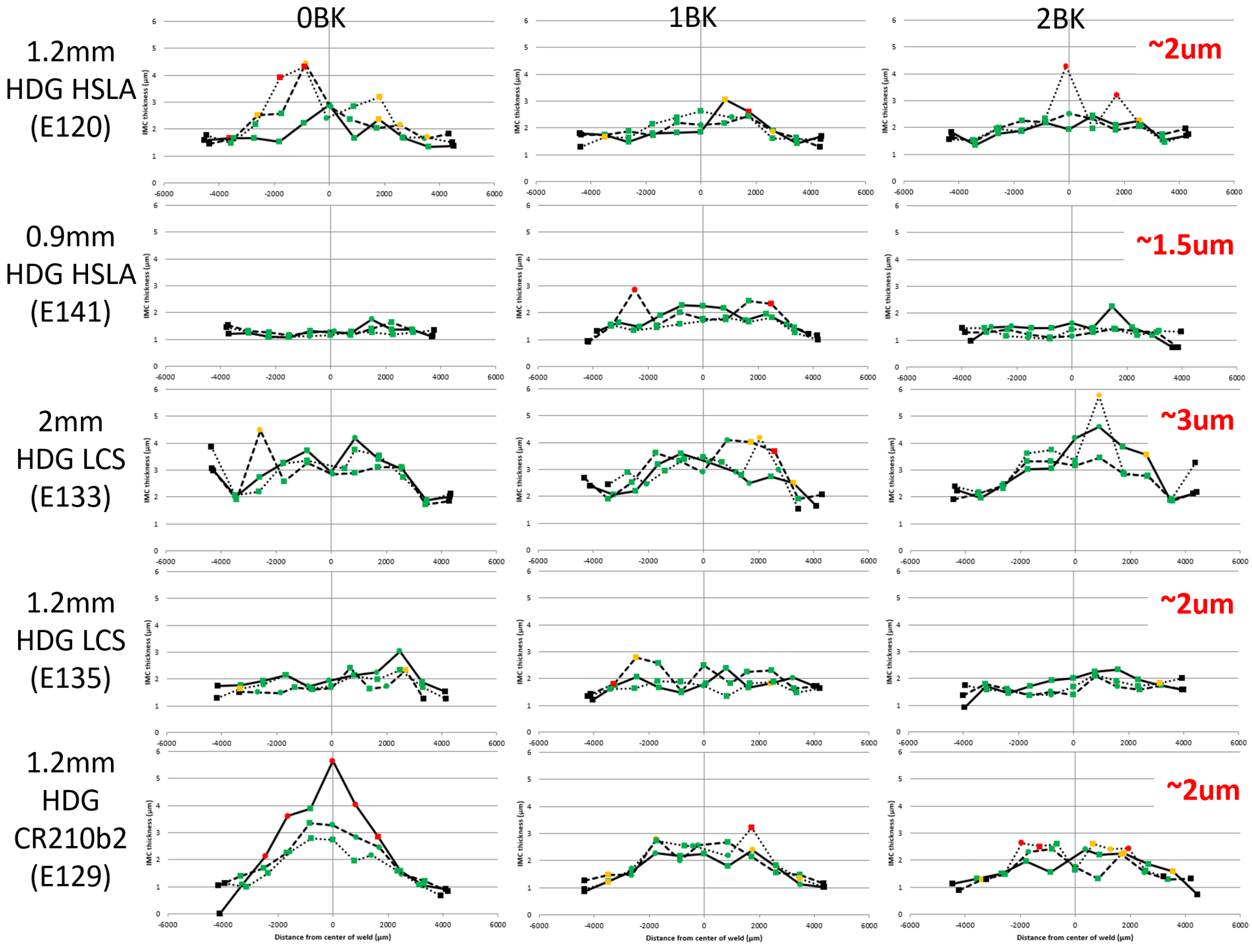

Figure 36. Measured thickness of intermetallic compound (IMC) layer along diameter of weld nugget for different welding conditions and material combinations. The numbers on the right side represent the average thickness of IMC layers.

Appendix D – Application of spherical tip indentation for property estimation

Spherical indenter was explored in extracting the stress-strain curves. Several load-depth curves were obtained from aluminum and steel base material regions, and two different methods (i.e., Tabor's method, Cao and Lu method) were adopted in estimating the stress-strain curves. Figure 37 and Figure 38 below show the comparison of stress-strain curves estimated from spherical indentation test with experiments for aluminum and steel based on the two methods.

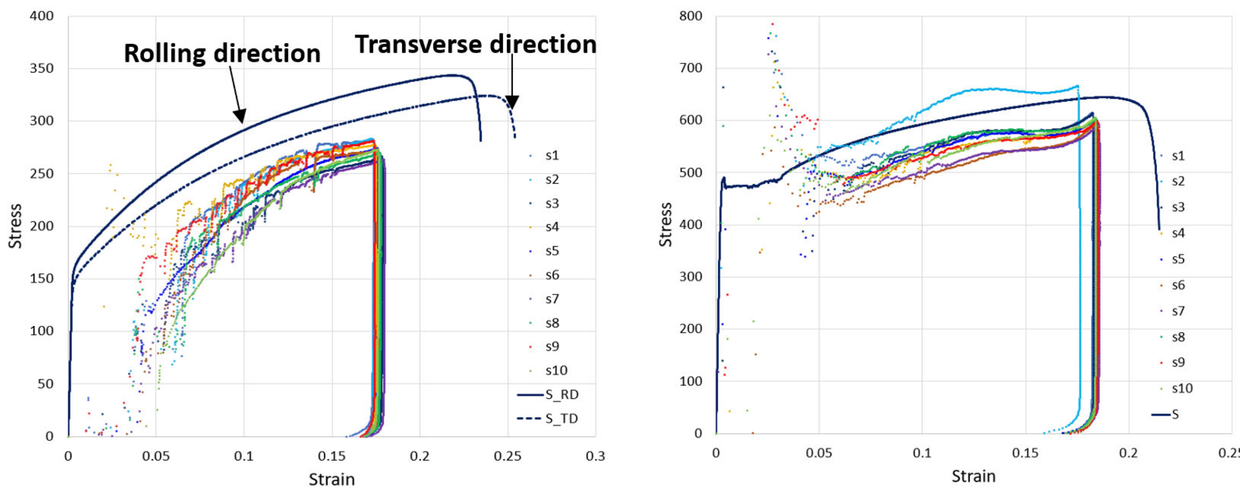

(a) (b)

Figure 37. Comparison of stress-strain curves estimated from spherical indentation test with experiments for (a)aluminum and (b) steel. (Based on Tabor relation).

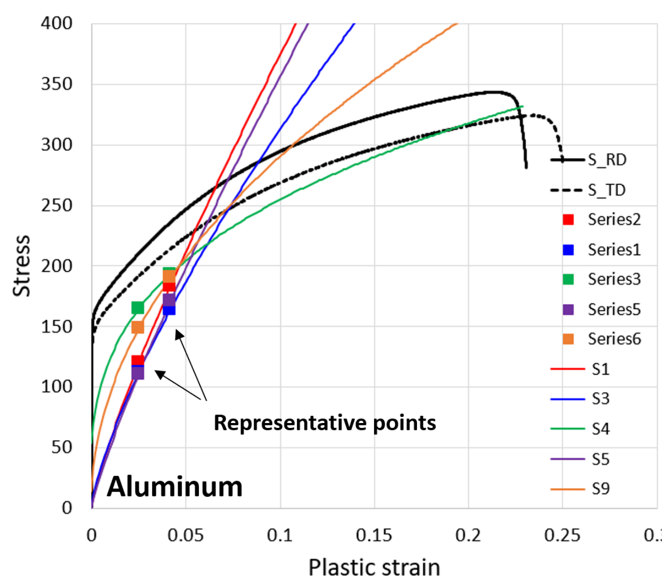

Figure 38. Comparison of stress-strain curves estimated from spherical indentation test with experiments for aluminum. (Based on Cao and Lu Method (Cao and Lu, 2004).

Appendix E – Application of finite element modeling for property estimation

Finite element modeling method was explored to examine the feasibility of using this method to back-estimate the material's stress-strain curves from load-depth curves. Two-dimensional (2D) axisymmetric and three-dimensional (3D) models were generated with different types of indenter tips (i.e., Berkovich tip, spherical tip and flat tip). Figure 39 below shows some examples of the generated 3D models with different tips. For these models, experimentally obtained stress-strain curves in Figure 40(a) below are used as the material input properties. Figure 40(a), Figure 40(b) and Figure 40(c) below show the comparison of load-depth curves obtained from simulations with experimental ones for different tips.

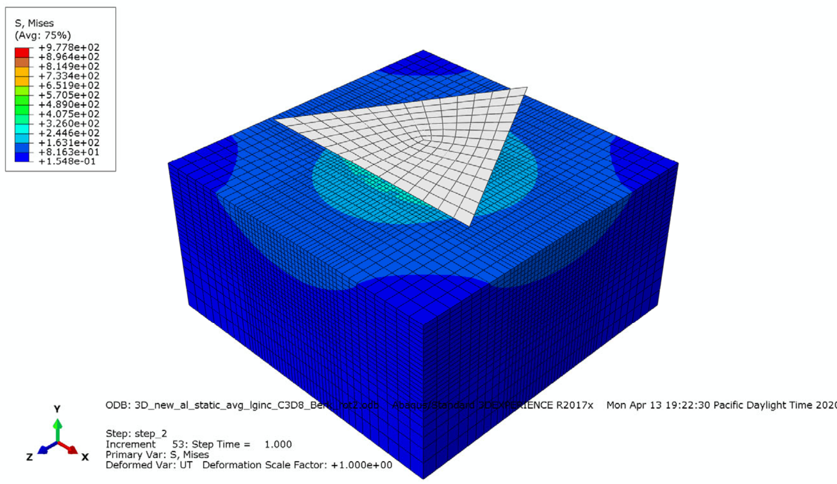

(a)

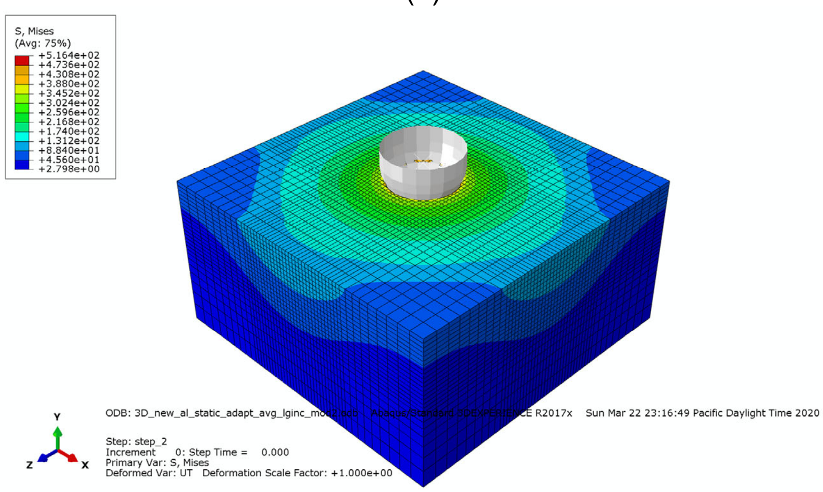

(b)

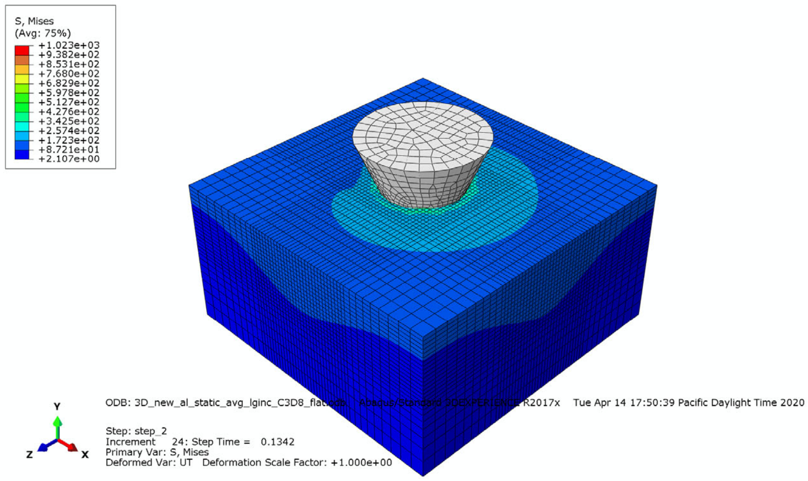

(c)

Figure 39. Finite element models for indentation simulations with (a) Berkovich tip, (b) spherical tip and (c) flat tip.

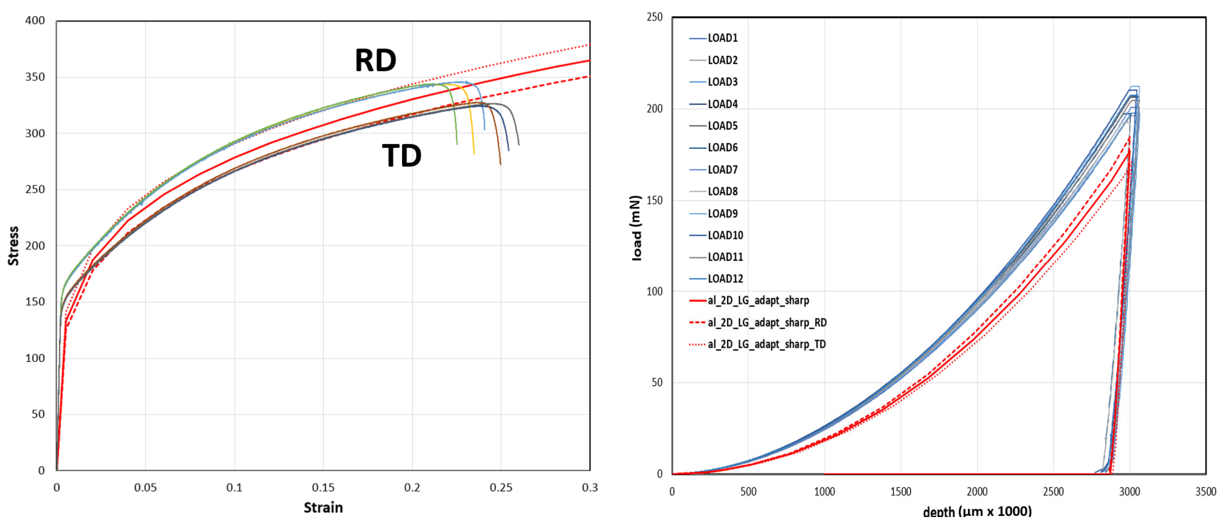

(a) (b)

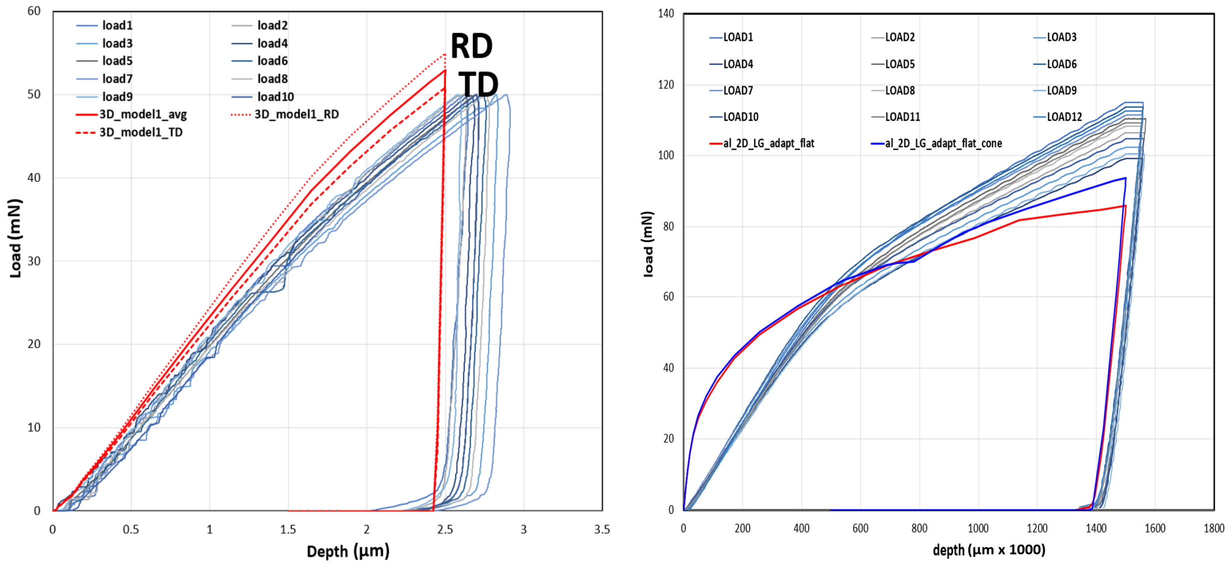

(c) (d)

Figure 40. (a) Aluminum input stress-strain curves for indentation simulations and comparison of load-depth curves obtained from simulations with experimental ones for (b) Berkovich tip, (c) spherical tip and (d) flat tip.

Pacific Northwest
National Laboratory

902 Battelle Boulevard
P.O. Box 999
Richland, WA 99354
1-888-375-PNNL (7665)

www.pnnl.gov